

University of Louisville

ThinkIR: The University of Louisville's Institutional Repository

Electronic Theses and Dissertations

8-2017

Applications of polarized metallic nanostructures.

Jasmin Beharic
University of Louisville

Follow this and additional works at: <https://ir.library.louisville.edu/etd>



Part of the [Electrical and Computer Engineering Commons](#)

Recommended Citation

Beharic, Jasmin, "Applications of polarized metallic nanostructures." (2017). *Electronic Theses and Dissertations*. Paper 2753.
<https://doi.org/10.18297/etd/2753>

This Doctoral Dissertation is brought to you for free and open access by ThinkIR: The University of Louisville's Institutional Repository. It has been accepted for inclusion in Electronic Theses and Dissertations by an authorized administrator of ThinkIR: The University of Louisville's Institutional Repository. This title appears here courtesy of the author, who has retained all other copyrights. For more information, please contact thinkir@louisville.edu.

APPLICATIONS OF POLARIZED METALLIC NANOSTRUCTURES

By

Jasmin Beharic

B.S., Electrical and Computer Engineering, University of Louisville, 2011
M.Eng., Electrical and Computer Engineering, University of Louisville, 2012

A Dissertation

Submitted to the Faculty of the
J.B. Speed School of Engineering of the University of Louisville
In Partial Fulfillment of the Requirements
For the Degree of

Doctor of Philosophy in Electrical Engineering

Electrical and Computer Engineering Department
University of Louisville
Louisville, Kentucky

August 2017

Copyright 2017 by Jasmin Beharic

All rights reserved

APPLICATIONS OF POLARIZED METALLIC NANOSTRUCTURES
By

Jasmin Beharic

B.S., Electrical and Computer Engineering, University of Louisville, 2011
M.Eng., Electrical and Computer Engineering, University of Louisville, 2012

A Dissertation Approved on

August 7, 2017

by the following Dissertation Committee

Cindy Harnett, PhD,
Dissertation Director

John Naber, PhD

Shamus McNamara, PhD

Stuart Williams, PhD

DEDICATION

To my family and friends

ACKNOWLEDGEMENTS

I would like to give specific thanks to Silvana Beharic, Hajrudin Beharic, Amer Beharic, Fadila Beharic, and Kate Moore for your help and support. I would also like extend my sincerest gratitude to Cindy Harnett for the opportunity to work with you and for your guidance and advice throughout this process.

ABSTRACT

APPLICATIONS OF POLARIZED METALLIC NANOSTRUCTURES

Jasmin Beharic

August 7, 2017

Gold nanostructures exhibit technologically useful properties when they are polarized in an electric field. In two projects we explore instances where the polarized metal can be used in real world applications. The first project involves gold nanoparticles (GNP) for use in light actuated microelectromechanical systems (MEMS) applications. Although the GNPs were originally designed for volumetric heating in biomedical applications, we treat them as a thin film coating, opening the door for these particles to be used in MEMS applications. This work characterizes the thermal properties of gold nanoparticles on surfaces for spatially-targeted thermal actuation in MEMS systems. The second project deals with metalized nanopore membranes for use in microfluidic applications. For this project, several models and experiments were performed on electroosmotic flows driven by charge separation at polarized nanopore surfaces. Until this work, the flow-through geometry remained unexplored for induced charge electroosmotic flow (ICEO).

TABLE OF CONTENTS

DEDICATION	iii
ACKNOWLEDGEMENTS	iv
ABSTRACT	v
LIST OF FIGURES	viii
CHAPTER I:	
INTRODUCTION	1
1.1 Background on thermally responsive “pop-up” structures	2
1.2 Background on bistable beams	4
1.2.1 Macroscale Bistable Beams	5
1.3 Gas Flow sensor	8
1.3.1 Flow Experiments	9
1.3.2 Results	10
1.4 Light-Driven Microactuation Using GNPs	12
CHAPTER II:	
LIGHT-POWERED MICROSTRUCTURES USING METAL NANO ABSORBERS	13
2.1 Gold Nanoparticle Background	13
2.1.1 GNP Shape Dependence: Spheres	15
2.1.2 GNP Shape Dependence: Rods	16
2.1.3 GNP Shape Dependence: Plates	19
2.1.4 GNP Synthesis	20
2.2 Light actuated MEMS	22
2.2.1 Dual Laser Heating Experiments	22
2.2.2 Light Actuated Bistable Structure	24
2.2.3 Polyimide Devices	26
2.2.4 Bulk Coating/Microfluidic GNP Patterning	27
2.3 GNP Thermal Stability	32
2.3.1 Bulk GNP Thermal Stability Experimental Setup	32
2.3.2 Bulk GNP Thermal Stability Results	34

2.3.3 DDSCAT	36
2.3.4 Single GNP Thermal Stability	38
2.3.5 Thermal stability discussion	40
2.3.6 Light actuated cantilevers	42
CHAPTER III:	
INDUCED CHARGE ELECTRO-OSMOSIS	44
3.1 ICEO Background	44
3.2 ACEO Background	45
3.3 Obstacle ICEO/ACEO	45
3.3 Applications of ICEO at membranes	47
3.3.2 Soft Robotics	48
3.3.3 A gap in the literature	48
CHAPTER IV:	
ALTERNATING CURRENT ELECTRO-OSMOTIC PUMPING AT ASYMMETRICALLY METALLIZED POROUS MEMBRANES	51
4.1 Flow-through ICEO Background	52
4.2 ICEO Device	55
4.2.1 Fabrication	55
4.2.2 Fabrication Limitations/Characterization	56
4.3 Experimental Results	59
4.3.1 Theoretical Expectations	59
4.4 Measurements	64
4.4.1 Simulations	66
4.4.2 Pressure Measurement Results	67
4.4.3 Control Experiments	72
CHAPTER V:	
CONCLUSIONS AND FUTURE WORK	76
5.1 Light Actuated MEMS - Conclusions	76
5.2 Light Actuated MEMS- Future work	77
5.3 Membrane ICEO - Conclusions	78
5.4 Membrane ICEO Future Work	79
5.5 Conclusions- Applications of polarized metallic nanostructures in electric fields	80
REFERENCES	82
APPENDIX A	93
CURRICULUM VITAE	97

LIST OF FIGURES

Figure 1: Example of Out-of-Plane Structure	3
Figure 2: Different possible structures using mismatched thermal expansion coefficient bilayers	4
Figure 3: (A) Setup for experiments with beams having a support width of 5 cm and symmetric end angles (B) Experimental results and prediction for thin plastic and metal strips	6
Figure 4: Fabrication diagram for the cleanroom processes	7
Figure 5: SEM view of the bistable windowpane structures, released to one of two states	8
Figure 6: Picture of the wind tunnel used for experiments with the wind sensor, with the top removed to change out the test chip	10
Figure 7: (A) Experimental data on critical flow rate vs side length, and model. (B) Linearized flow rate data for extracting the model fitting parameter	11
Figure 8: Plasmon oscillation for a spherical particle	13
Figure 9: Absorbance spectrum of oxygenated and deoxygenated blood, and water	14
Figure 10: Example Absorbance Spectra from Literature for spherical GNPs	16
Figure 11: The electron cloud oscillation under an electric field	17
Figure 12: Example Gold Nanorod Absorbance Spectra from Literature	19
Figure 13: Extinction spectrum of gold nano-shells (A) Exact calculation from Mie theory (B) Calculation using DDA	20

Figure 14: Typical absorption profile for GNP plates	21
Figure 15: Dual Laser Experimental results (A) Temperature response sample under 808nm Laser (B) Temperature response sample under 915 nm laser (C) Percent change in peak temperature	23
Figure 16: Windowpane device deflection under pulsating laser	25
Figure 17: PI/oxide bilayer cantilevers curling up from a silicon substrate	27
Figure 18: Fabrication diagram for microfluidic patterning of GNP devices	29
Figure 19: (A - D) Scanning electron micrograph images of a GNP coating deposited onto an APTS-covered silicon surface using a microfluidic channel (E) Optical micrograph of the array	30
Figure 20: Microfluidic patterning GNP process (A) Two different wavelength GNP patterned in close proximity to each other (B) Alignment mark for photolithography (C) Cantilevers alighted on top of the GNPs.	31
Figure 21: Bulk GNP thermal stability sample preparation and data collection locations	34
Figure 22: Absorbance profile for bulk heating experiments at 350 C	35
Figure 23: Average Absorbance Peak post heating	36
Figure 24: DDSCAT Simulation Shapes (A) Triangle with sharp edges (B) Triangle with rounded edges	37
Figure 25: Experimental and simulation results for single GNP scattering	38
Figure 26: Method for Finding Individual GNPs using Darkfield Microscopy	39
Figure 27: Single GNP percent shift for triangular particles	40
Figure 28: PI cantilevers moving under laser light (A) laser off (B) laser on	42
Figure 29: Side-by-side GNP/control cantilever arrays	43
Figure 30: Images taken from our previous work with flow in the plane of the page	46
Figure 31: Research on induced charge electroosmosis	49
Figure 32: Illustrates how asymmetry (right side) can drive nonzero flow around an obstacle or through a pore in an AC trans-membrane electric field	53
Figure 33: Fabrication Diagram for ICEO Membranes	56

Figure 34: Asymmetrically metallized nanopores fabricated by metallizing track-etched membranes	57
Figure 35: Cross sectional view of a membranes showing gold deposited along the side walls	58
Figure 36: Impedance calculations for obtaining voltage across membrane	59
Figure 37: Expected pressure output vs pore diameter	61
Figure 38: (A) Pressure-vs-voltage is nearly linear (B) Electron micrograph of membrane	63
Figure 39: Block diagram for data collection	64
Figure 40: Laser cut acrylic pressure measuring device	65
Figure 41: Flow Visualization Device	65
Figure 42: Simulation Visualizations and differential pressure validation	67
Figure 43: Device Voltage Response (A) Typical voltage-vs-time response for membranes with 1 micron pore diameters (B) Steady-state Pressure vs Voltage for membranes with different pore diameters	68
Figure 44: Pressure response to change in frequency	70
Figure 45: Average pressure for given frequency	70
Figure 46: Maximum Pressure vs pore diameter	71
Figure 47: Pressure measurements for control devices (A) positive electrode is facing metalized surface (B) positive electrode is facing non-metalized surface	72
Figure 48: Pressure measurements for control devices (A) Device with non-metalized membrane (B) Device with no membrane	73
Figure 49: Flow through experiments (A) DI water position before applied voltage (B) DI water position after applied voltage	74
Figure 50: Flow rate vs time for a 400nm membrane at 120Vrms	75
Figure 51: Pressure experiments with multiple membranes	79

CHAPTER I: INTRODUCTION

Gold (Au) has always been a valuable metal because of its unique physical properties. Gold is an attractive metal because of its thermal and electrical conductivity while resistant against oxidization, making it well-suited for applications in medicine and technology. Although the bulk properties of gold are useful, this project will focus on the nanoscale properties of gold which have been shown to diverge. These nanomaterials show promise in many areas such as drug delivery, microfluidics, and cellular manipulation. Further study and characterization are needed to achieve their full potential. In the following chapters, we will attempt to shed light on some of these properties to better understand their behavior. This dissertation will explore the behavior of gold nanostructures under different stimuli such as lasers, high temperatures, and electric fields. Two different projects will be discussed that explore how to incorporate these nanostructures into devices that will utilize these unique behaviors to convert electromagnetic energy into movement.

The first project involves gold nanoparticles (GNP) for use in light actuated microelectromechanical systems (MEMS) applications. Although the GNPs were originally designed for photo-thermal therapeutics in biomedical applications, we treat them as a thin film coating, opening the door for these particles to be used in MEMS

applications. This work characterizes the thermal properties of gold nanoparticles on surfaces for spatially-targeted thermal actuation in MEMS systems. We show that GNPs do increase the absorbance of laser energy; a side by side comparison of cantilevers with and without embedded GNPs showed greater deflection for cantilevers with GNPs than those without. The second project deals with metalized nanopore membranes for use in microfluidic applications. The nanostructures are placed in a fluid with a tangential electric field which induces motion in the medium using an electric bilayer. For this project, several models and experiments were performed on electroosmotic flows driven by charge separation at polarized nanopore surfaces. We successfully demonstrate flow driven by an AC field at an asymmetrically metallized nanoporous surface with 400 nm diameter pores. Until this work, flow-through geometry remained unexplored for induced charge electroosmotic flow (ICEO). For each project, this dissertation will provide a comprehensive background on the underlying physics governing the behavior of the structures involved. Additionally, the development of the techniques required to incorporate these structures into proof of concept devices will be chronicled, outlining the basis for future real-world applications.

1.1 Background on thermally responsive “pop-up” structures

Out of plane structures can be created by depositing two layers with different thermal expansion coefficients onto each other [1]. The strain mismatch in the structure between the two layers causes the structure to pop-up once it is released from the surface.

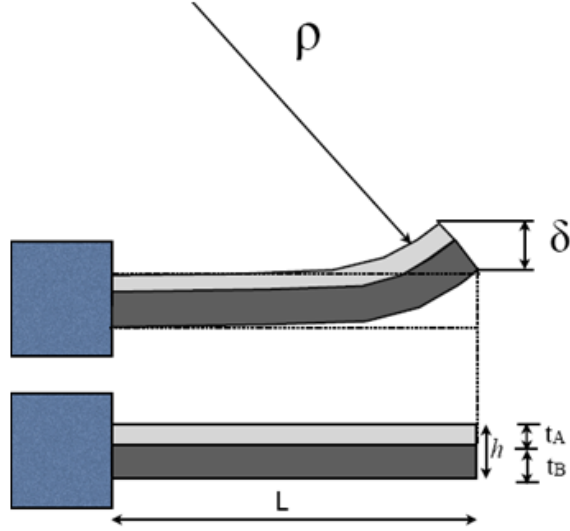


Figure 1: Example of Out-of-Plane Structure

$$\frac{1}{\rho} = \frac{6(1+m)^2(\alpha_B + \alpha_A)(\Delta T)}{h[3(1+m)^2 + (1+mn)(m^2 + 1/(mn))]} \quad (1)$$

$$m = \frac{t_A}{t_B} \quad (2)$$

$$n = \frac{E_A}{E_B} \quad (3)$$

$$h = t_A + t_B \quad (4)$$

Where the radius of curvature ρ is given by Equation 1[2], α_a and α_b are the thermal expansion coefficients, and ΔT is the change in temperature. This technique can be used to create simple out-of-plane structures such as cantilevers or more complex structures with bistability. Both of these structures are utilized in this project. By changing the temperature (ΔT), the radius of curvature can be changed. It is this effect which will be used in this

work to create light actuated MEMS. In using this technique, several interesting structures can be created.

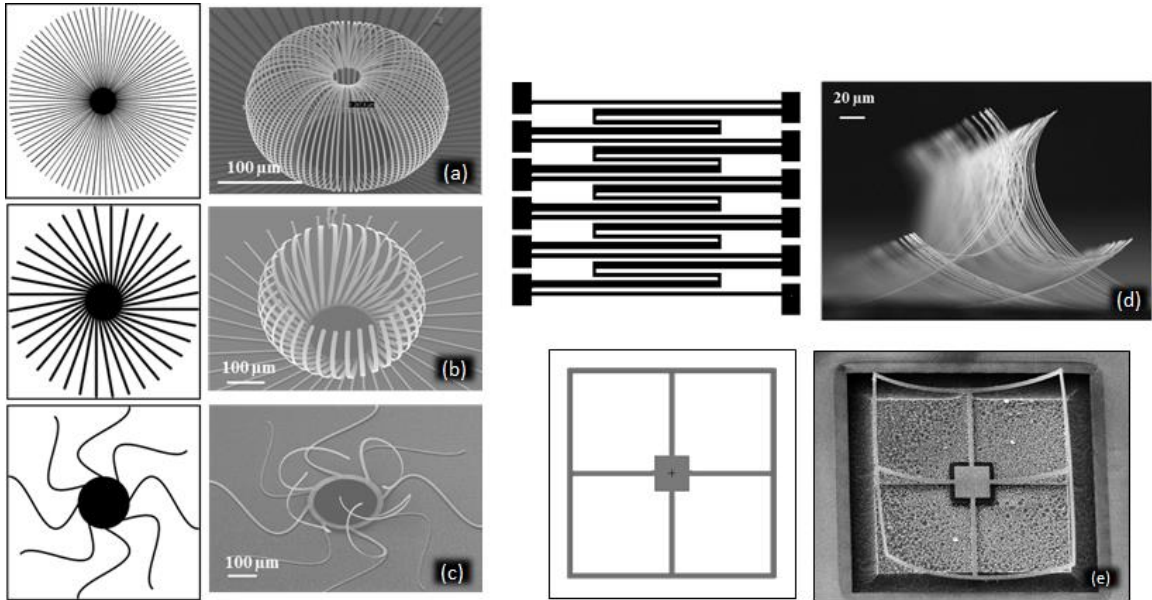


Figure 2: Different possible structures using mismatched thermal expansion coefficient bilayers [3].

The structure which is of most interest for this project is the structure in Figure 2 (e) which is a bistable geometry.

1.2 Background on bistable beams

The buckled beam theory can be used to create bistable structures that hold their shape without energy applied [4,5,6]. Multiple stable shapes are allowed, potentially leading to MEMS that can be programmed into shape by the temporary application of power. The bistable geometry minimizes power consumption while the actuator is at rest. The results in Figure 3(b) show that the critical angle measurements collapse to a single

shape for a variety of sample thicknesses, whether the material is metal (high modulus) or plastic (low modulus). Both metal and plastic beams show similar properties in the snap-through behavior, which is important because our micro scale experiments will also switch between different materials.

1.2.1 Macroscale Bistable Beams

A bistable mechanical structure can be formed by the compression of a thin ribbon-shaped beam. The mechanics are similar from the micron scale to the cm- and meter scale. The beams will “snap” from one state to another. Usually in macroscale applications the snapping is induced by pressure applied on the center of the beam, but we recently investigated the stability of cm-scale beams that had rotated endpoints [7] instead of applied pressure. This situation would apply at the microscale to thin-film compressed beams supported on a soft surface with changing curvature. Endpoint rotation could also be achieved by thermal actuation as described in Section 1.1. We determined that the snap-through rotation angle is controlled chiefly by the amount of compression in the beam, which in microscale processes can be “programmed” by deposition temperatures.

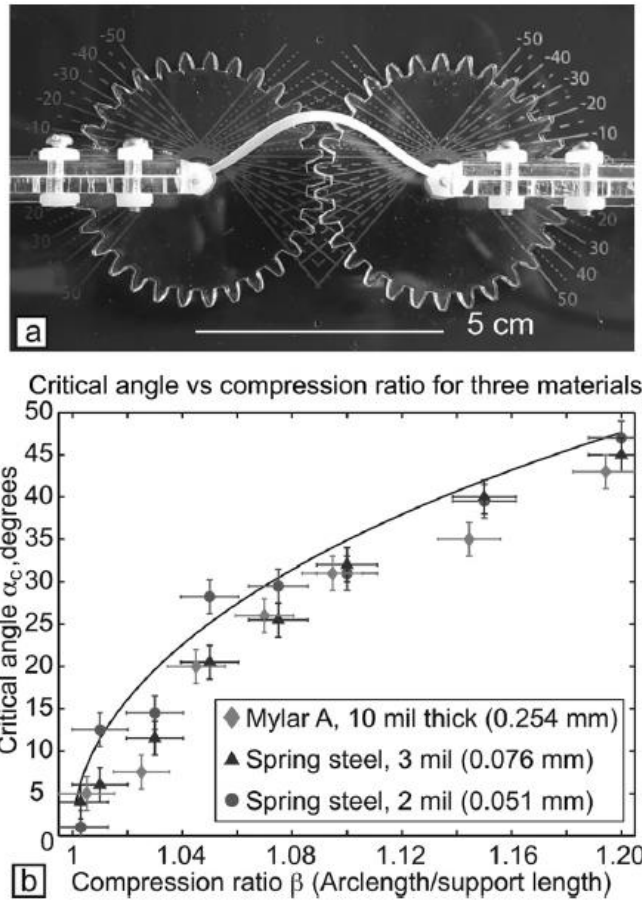


Figure 3: (A) Setup for experiments with beams having a support width ($2w$) of 5 cm and symmetric end angles a . (B) Experimental results and prediction for thin plastic and metal strips. Snap-through angle is a function of the compression ratio b , and does not depend on absolute scale or material properties as long as assumptions are met.

1.2.2 Bistable Out-of-Plane Microstructures

Bistable structures have been used in many applications such as switches [8,9], relays [10], and energy harvesters [11]. The bistable microstructure presented in this work, referred to as a “windowpane”, is a unique structure with two stable states that the device

will release into randomly. Due to the symmetry of the windowpane it can curl along either of the two axes with equal strain energy in either state, with the device showing no observed initial orientation preference. The device can be forced to release into a preselected state by adding dots to the beams which slightly delays the release of the device. This bistable structure can be used as a sensor that only needs power when determining which state the bistable structure is in.

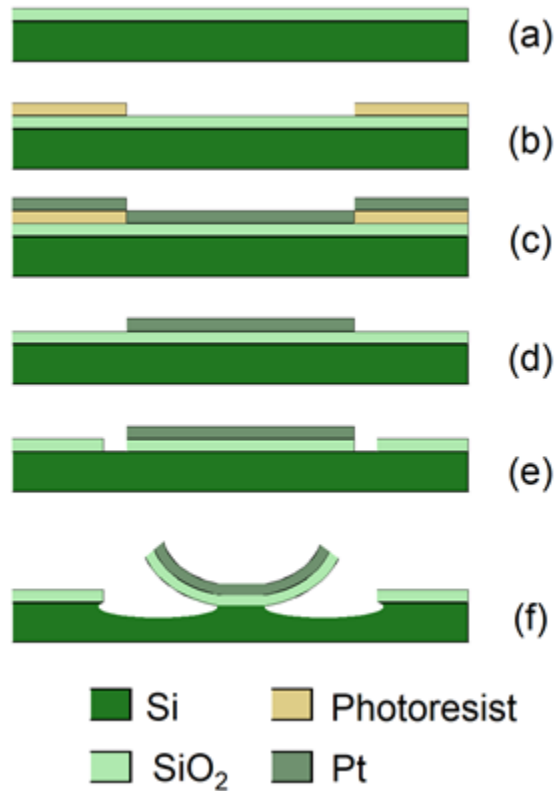


Figure 4: Fabrication diagram for the cleanroom processes used to fabricate the devices.

The fabrication processes in Figure 4 depict a standard 4 in silicon wafer which acts as the substrate for material deposition. The bilayers required for creating the pop-up geometry are SiO₂ and Pt. The SiO₂ layer is thermally grown to a size of 500 nm (Figure

4A). Photoresist is then spun on and patterned using photolithography (Figure 4B). Next, a 10 nm titanium adhesion layer and a 90nm platinum layer is deposited by sputtering (Figure 4C). Lift-off is used to remove the Pt leaving the windowpane shape behind (Figure 4D). The SiO₂ is then etched to create a path to the Si (Figure 4E). To release the structure, an isotropic XeF₂ etch is used to undercut the device and release it from the surface (Figure 4F). The final resulting structure curls to one of two states as pictured in Figure 5 from a scanning electron microscope (SEM).

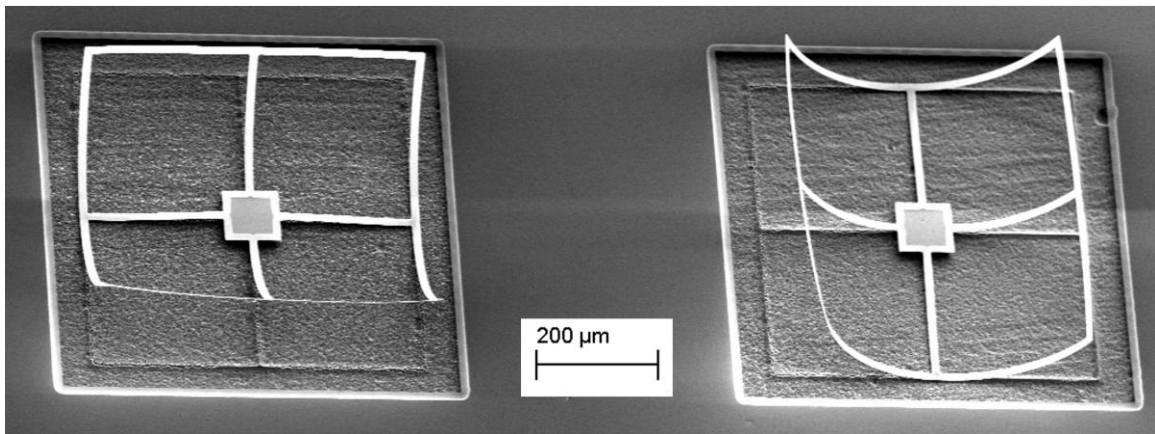


Figure 5: SEM view of the bistable windowpane structures, released to one of two states.

1.3 Gas Flow sensor

To verify the bistability of this design, mechanical switching was activated using gas flow. This phenomenon was used as the basis for a flow sensor because the variables that govern the switching behavior are the side length and the flow velocity of the air applied to the device [12]. This switching phenomenon is repeatable and since the device requires no power to maintain the stable state, the sensor only requires power during the sensing stage. Experimental measurements showing the stability state switching response

of the device under different flow conditions are presented. Results show that larger devices switch at slower flow velocities and that the stability state switching threshold can be calibrated to a desired gas flow rate. Structures with a square side length of 550 μm to 700 μm at 25 μm intervals were fabricated to characterize the effect of surface area on the lift force, and therefore flow speed. The lift force is:

$$F_D = \frac{1}{2} \rho v^2 c_D A \quad (5)$$

The lift force (F_D) is proportional to the density of the medium (ρ), the flow velocity squared (v^2), the lift coefficient (c_D), and the surface area (A). In the following experiments, the force exerted by a given flow velocity was varied by modifying the side length parameter, which affects the surface area (A).

1.3.1 Flow Experiments

A micro wind channel was created for testing these devices. Figure 6 shows the micro wind tunnel opened for exchanging the device. Pressurized N_2 was used for the flow medium. The gas was applied to a single channel with a centrally situated device. Two wind channels are at 90 degrees to allow testing in both switching directions of the bistable structure. The devices were optically monitored via an Olympus BX-71 microscope for a change in state with a one second air burst at a known velocity. The device reliably switches in both directions at or above a flow speed threshold, depending on the geometry.

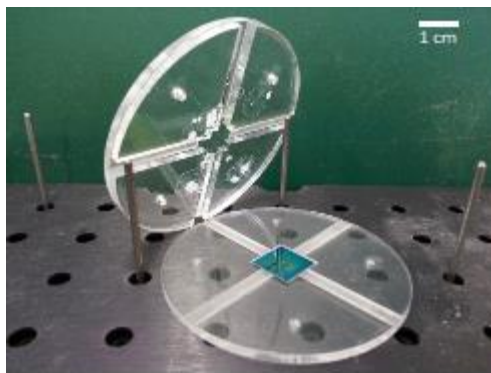


Figure 6: Picture of the wind tunnel used for experiments with the wind sensor, with the top removed to change out the test chip.

The wind tunnel in Figure 6 is laser cut out of three layers of 1/8th inch (3.175 mm) acrylic. Straight cut and raster modes are used to create the air channels and seating area for the device. The inlet and outlet channels are 5 mm wide with an approximate height of 3.2 mm including the raster etch. Plastic tubing is installed in these channels for airflow into and out of the system. The center device chamber is a 1 cm square with a height of 3.175 mm from substrate surface to the chamber ceiling. A 500 μm raster etch of the center base was included so the substrate surface was even with the chamber bottom. The air flow in the center device area is calculated to be laminar. The flow speeds with air used in this experiment, 5 to 10 LPM, suggest a Reynolds number range from 800 to 1700.

1.3.2 Results

The data points show that the air flow required to cause a state change is reduced as the surface area of the device increases (Figure 7A). The experimental data for side length and critical flow rate in Figure 7A are fit with a curve obtained using the model described in APPENDIX A. The data error range is derived from the accuracy of the

rotameter and pressure regulator. Figure 7B shows a linearization of the measured critical flow rate data to solve for the fitting parameter. The constant was obtained as the slope of the line fit to the data in Figure 7B, and was the single fitting parameter used to connect the model to the data.

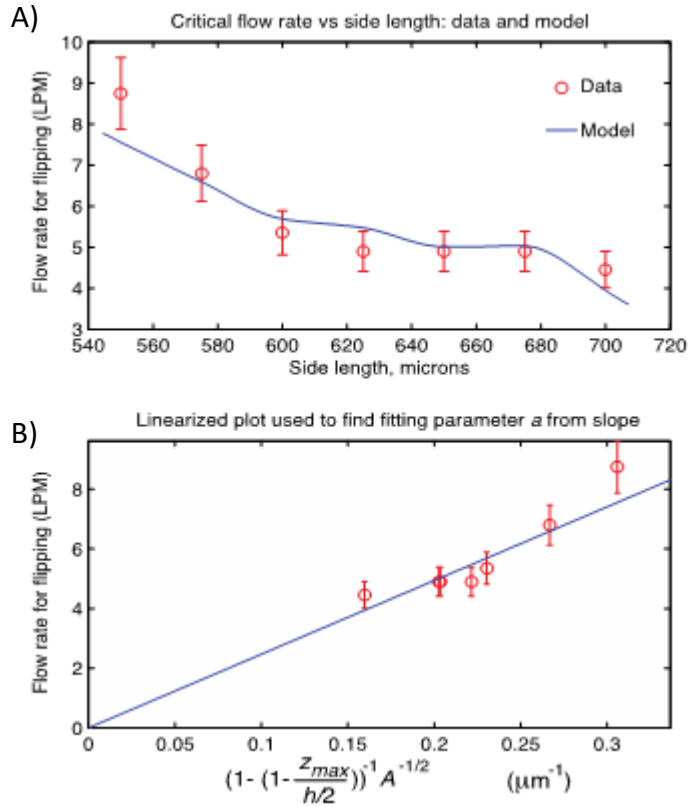


Figure 7: A) Experimental data on critical flow rate vs side length, and model.

B) Linearized flow rate data for extracting the model fitting parameter.

Larger windowpanes can be expected to switch at lower flow speeds for several reasons. First, elongating the side length increases the surface area of the structure. Drag force is proportional to this area for a constant air speed, so larger devices experience more force. Second, the structure demonstrates greater compliance as the beam length increases.

Third, a larger device extends higher into the channel and interacts with faster-flowing streamlines. The resemblance of the data in Figure 7B to the model, which ignores variation in snap-through force with L , suggest that the area and height are more important than the spring constant in setting the threshold flow rate over the size range studied.

1.4 Light-Driven Microactuation Using GNPs

Currently most of the research with GNPs is focused on cancer therapy. The GNPs are used as photothermal treatments for directly attacking the cancer cells and reducing their size [13], and also in imaging as a contrasting agent [14]. Since the particles can be functionalized to attach to cancer cells, they have been used as a drug delivery system [15,16]. Usually these particles are distributed throughout a fluid or tissue sample. However, in this work we applied the GNPs in a new environment: on planar surfaces and on materials such as silicon and glass found in MEMS devices.

CHAPTER II:

LIGHT-POWERED MICROSTRUCTURES USING METAL NANO ABSORBERS

2.1 Gold Nanoparticle Background

The absorbance of gold nanoparticles (GNP) has been attributed to the collective oscillation of the free electrons in the conduction band, which is known as surface plasmon oscillation (SPO). SPO occurs when the GNP are exposed to light. The incident electric field acts on the free electrons in the GNP, creating a polarized effect as shown in Figure 8. Due to the Coulomb attraction between the electrons and nuclei of the GNP, the electron cloud will shift back to the opposite side which creates the plasmon resonance [17].

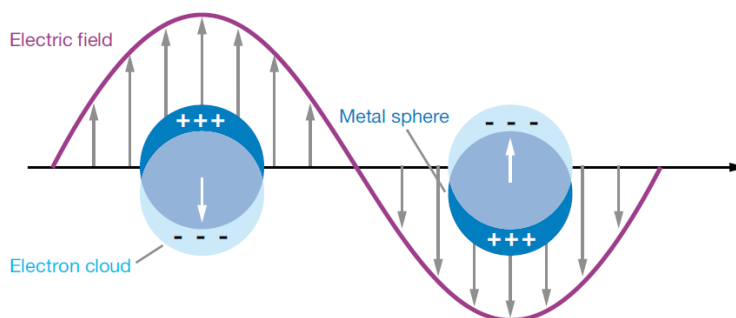


Figure 8: Plasmon oscillation for a spherical particle [17]

The GNPs are well-suited for in vivo applications because of their biocompatibility, inertness, drug loading potential, and ability to tune their wavelength in the Near-Infrared

(NIR) window. The NIR window (650-1450 nm) is where light has its deepest penetration [18,19] into tissue while having low absorbance coefficient for blood cells and other biological materials. Since we use GNPs, which are between 700 nm and 900 nm, we are well within NIR window range. An example of the NIR window absorbance spectrum can be seen in Figure 9. The figure shows the absorbance of oxygenated blood and deoxygenated blood which fits in well with the GNPs that we are using.

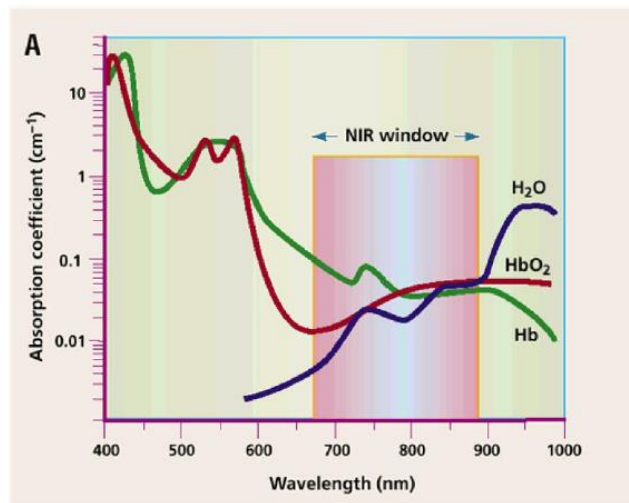


Figure 9: Absorbance spectrum of oxygenated and deoxygenated blood, and water [20]

GNPs can be created in many different sizes ranging from 2 to 250 nm [21] and shapes such as spheres [22], rods [23], and plates [24,25]. All off these can be used to fine tune the absorbance peaks of the GNPs to a high degree of accuracy.

2.1.1 GNP Shape Dependence: Spheres

The absorbance spectrum for GNPs is strongly dependent on the shape of the particles. There are several types of GNPs including spheres, rods, and differently shaped plates (hexagons, triangles). Spherical particles generally absorb in the lower ranges of the NIR window around the 650 nm wavelength [26]. For spherical particles, an exact solution to the absorbance as a function of wavelength can be calculated using Mie theory, derived from the Maxwell equations with the correct boundary conditions. The equations reduce down to Equation 6 which is given below.

$$\sigma_{ext} = 9 \frac{\omega}{c} \epsilon_m^{3/2} V_0 \frac{\epsilon_2(\omega)}{[\epsilon_1(\omega) + 2\epsilon_m]^2 + \epsilon_2^2(\omega)} \quad (6)$$

Where V is the volume of each individual particle, ϵ_m is the dielectric constant of the medium, c is the speed of light, ϵ_1 and ϵ_2 are the dielectric function of the material, ϵ_1 is the real part of the dielectric function while ϵ_2 is the imaginary part. According to Equation 6, the only size dependent variable is volume which is proportional to the particle diameter. However, this result does not fully line up with the experimental results seen in the literature (Figure 10). This discrepancy has been attributed to the change in the dielectric function ϵ_1 with increasing particle diameter.

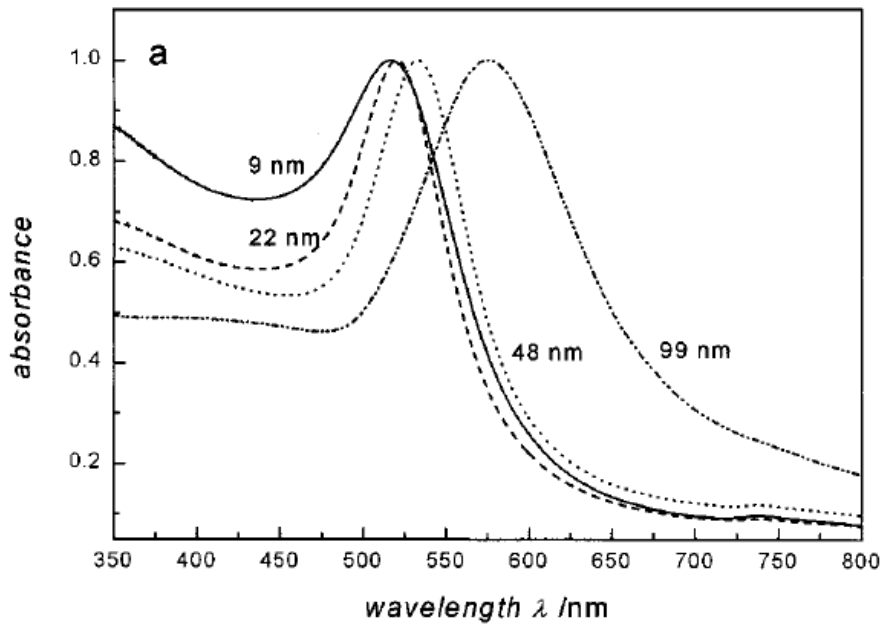


Figure 10: Example Absorbance Spectra from Literature for spherical GNPs [27]

2.1.2 GNP Shape Dependence: Rods

GNP rods work similarly to the spherical particles, with a resonance driven by an external electric field. However, due to the asymmetric shape of the rods the SPO has both a longitudinal and a transverse component.

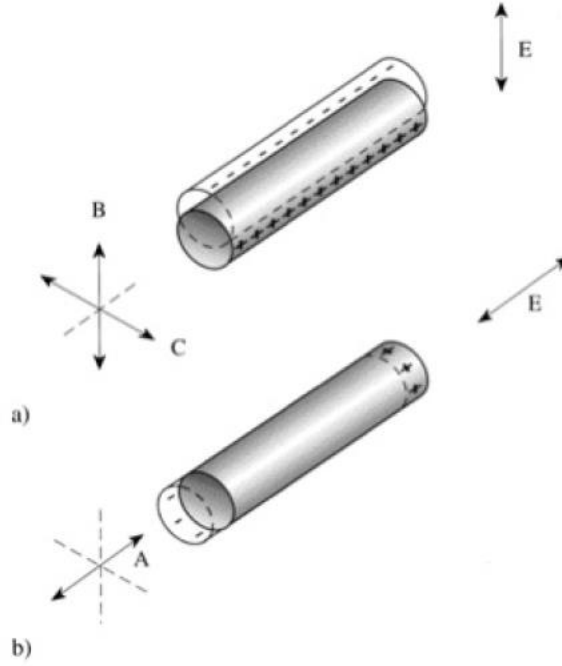


Figure 11: The electron cloud oscillation under an electric field (a) the transverse oscillation along the B or C axis and (b) the longitudinal oscillation along the A axis [28].

Since the electron cloud can oscillate in two directions, there are two distinct absorbance peaks present in the spectrum. GNP rods also have an exact solution by modifying the Mie theory with a geometric factor. The extinction coefficient is described by Equation 7 [29].

$$\gamma = \frac{2\pi N V \epsilon_m^{3/2}}{3\lambda} \sum_j \frac{(1/P_j^2)\epsilon_2}{(\epsilon_1 + \frac{1-P_j}{P_j}\epsilon_m)^2 + \epsilon_2^2} \quad (7)$$

In the equation, N is the number of particles per unit volume, V is the volume of each individual particle, ϵ_m is the dielectric constant of the medium, λ is the light wavelength, ϵ_1 and ϵ_2 are the dielectric function of the material, ϵ_1 is the real part of the dielectric function, while ϵ_2 is the imaginary part. P_j is the depolarization factor for the three axes A , B , and C of the GNP rods. The depolarization factor is defined by the P_A , P_B , and P_C which are described in Equations 8 and 9 below. The aspect ratio of the nanorods is in the e term with B/A , which can be seen in Equation 10.

$$P_A = \frac{1 - e^2}{e^2} \left[\frac{1}{2e} \ln \frac{1 + e}{1 - e} - 1 \right] \quad (8)$$

$$P_B = P_C = \frac{1 - P_A}{2} \quad (9)$$

$$e = \sqrt{1 - \left(\frac{B}{A}\right)^2} \quad (10)$$

A solution to the equations can be seen in Figure 12A with clearly defined peaks for the transverse oscillation and the longitudinal oscillation. The aspect ratio plays an important role in the absorbance of the GNPs, which can be seen in Figure 12B with different aspect ratios plotted against each other.

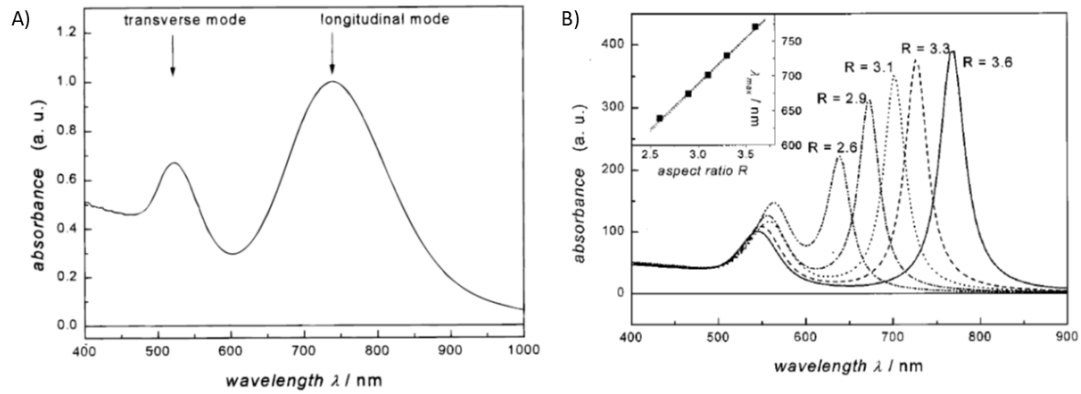


Figure 12: Example Gold Nanorod Absorbance Spectra from Literature [30]; note second peak caused by asymmetry in the rod-shaped particles.

2.1.3 GNP Shape Dependence: Plates

Unlike spheres and rods, nanoplates do not have an exact mathematical solution. Because there is no exact solution to the GNP plates, other approaches are needed to calculate the scattering and absorption properties of the particles, such as the discrete-dipole approximation (DDA). DDA can be used to calculate the properties of any arbitrary shape by segmenting the object into an array of polarizable elements. By applying a localized electric field, each point acquires a dipole moment. This can be used to get the far-field properties such as extinction efficiencies, and also near-field properties such as the electric field near the particle surface [32,32]. Knowing the properties of the electric field near the particle surface allows for the calculation of the scattering and absorption properties of the particles. Because there is no exact solution to this structure it is difficult to determine the accuracy of DDA, but this method has been tested against known solutions and shows fairly close agreement. The results of one such study can be seen in Figure 13.

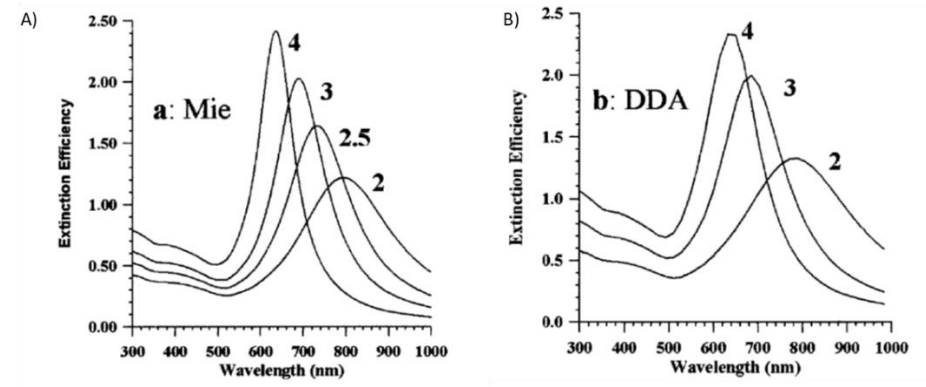


Figure 13: Extinction spectrum of gold nano-shells A) Exact calculation from Mie theory
 B) Calculation using DDA [33].

2.1.4 GNP Synthesis

Gold nanoparticles with precisely controlled nIR absorption are synthesized by one-step reaction of chloroauric acid and sodium thiosulfate in the presence of a cellulose membrane. The NIR absorption wavelengths and average particle size increase with the increasing molar ratio of $\text{HAuCl}_4/\text{Na}_2\text{S}_2\text{O}_3$. The gold salt used is hydrogen tetrachloroaurate (III) trihydrate 99.99% ($\text{HAuCl}_4 \cdot 3\text{H}_2\text{O}$) purchased from Alfa Aesar. A 1.72 mM solution is prepared with DI water and protected from light with aluminum foil. A 32.6 ml volume of the 1.72 mM gold salt solution is combined with 7.4 ml of a 3 mM sodium thiosulfate pentahydrate solution ($\text{Na}_2\text{S}_2\text{O}_3 \cdot 5\text{H}_2\text{O}$; purchased from Sigma-Aldrich) to perform the reactions for synthesizing the nIR GNPs. A 12 kDa Molecular Weight Cut-Off (MWCO) membrane (Flat Width $\frac{1}{4}$ 43 mm) from Sigma-Aldrich is cut to the desired length (150 mm for 770 nm GNPs and 100 mm for 940 nm GNPs), then one end of the tube is closed with a weighted dialysis clip and filled with the gold salt solution. The

$\text{Na}_2\text{S}_2\text{O}_3$ solution is then added into the tube via pipette, followed by mixing the solution within the membrane by manually stirring with the tip of the pipette and aspirating with the pipette pump. Subsequently, air is removed from the tubing and the other end of the membrane is clipped. The sealed tube is placed in an 8 L beaker filled with 7 L of DI water and a stir bar at the bottom of the beaker rotating at 200 rpm. This mixture is allowed to react for 1 hour. Particle batches, composed of various pseudo-spheres and anisotropic nanostructures, are dispersed in 8% PVP by weight solution to make the polymer GNP mixture used for this experiment [34]; a typical optical absorption spectrum appears in Figure 14.

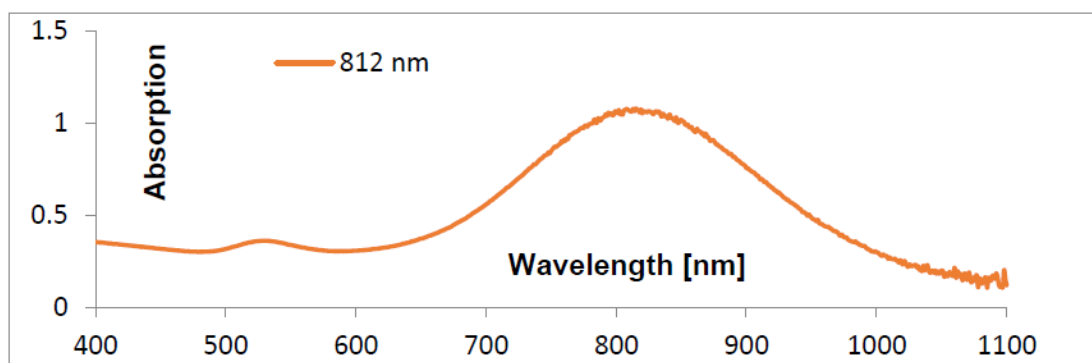


Figure 14: Typical absorption profile for GNP plates.

2.2 Light actuated MEMS

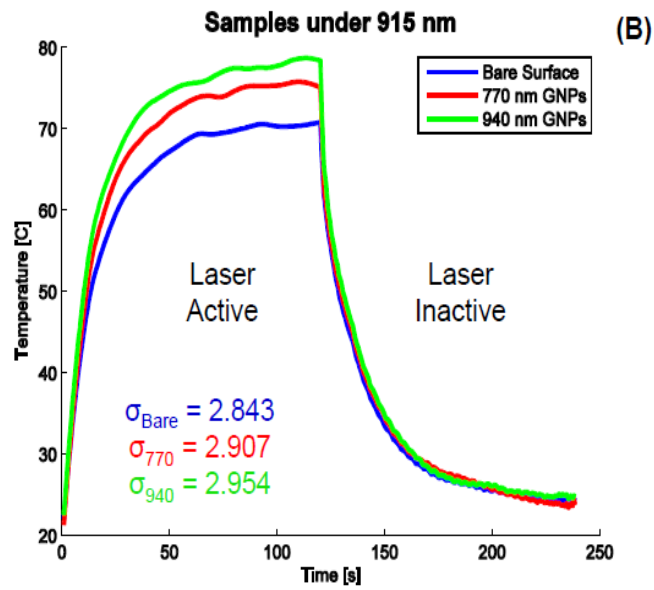
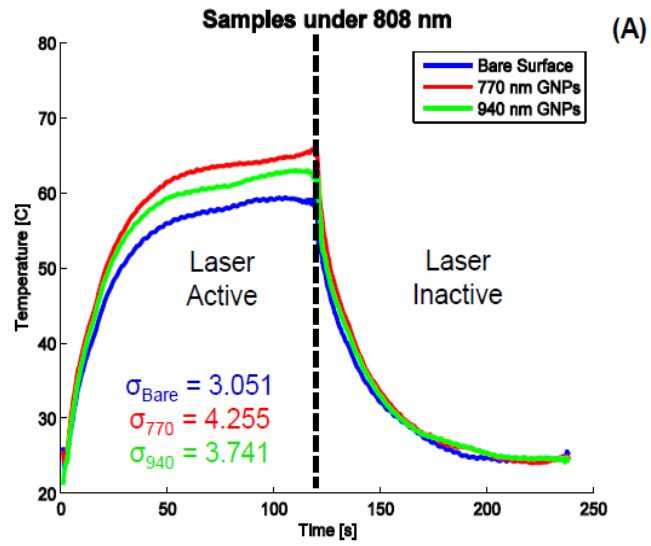
Light has been used in the past to create motion with photosensitive material [35], and some have also used GNPs in their design [36]. However, these previous applications have been on the macro scale, as their use in micro scale applications still remains under explored.

MEMS devices have shown great promise in in vivo applications because of their small size and versatility. The ability to create small-scale actuators and pumps could have many applications in biomedicine in the form of cell manipulators and drug release. Most of these devices use wires or have toxic batteries [37]. Light-actuated MEMS on the other hand present an opportunity for a wireless device which does not require batteries or wires to function.

2.2.1 Dual Laser Heating Experiments

One of the benefits of using GNP as a heating source is the ability to use multiple variations of wavelength particles on the same device. This section will explore the results of dual wavelength laser experiments to show the response of GNP when tuned to different laser wavelengths.

This section demonstrates a basis for designing light-powered MEMS with a wavelength specific response. This is accomplished by patterning surface regions with a thin film containing gold nanoparticles that are tuned to have an absorption peak at a particular wavelength. The heating behavior of these patterned surfaces is selected by the wavelength of the laser directed at the sample. This method also eliminates the need for wires to power a device.



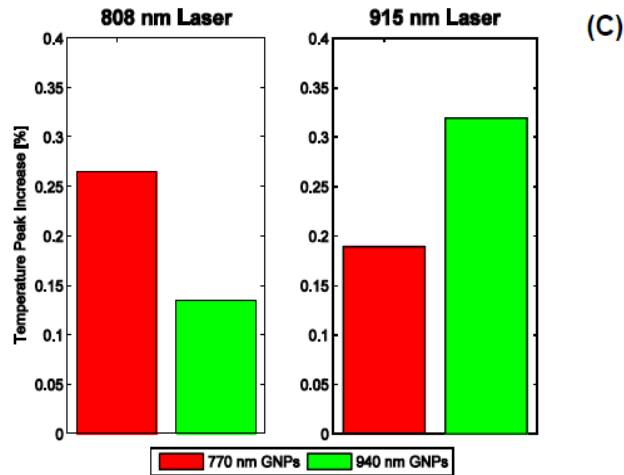


Figure 15: Dual Laser Experimental results [38] A) Temperature response sample under 808nm Laser B) Temperature response sample under 915 nm laser C) Percent change in peak temperature

As we can see in the experimental results shown in Figure 15A, the 770 nm GNPs heat more when illuminated with an 808 nm laser than with a 915 nm laser. Additionally, as we can see in the results shown in Figure 15B, the 940 nm GNPs respond better to the 915 nm laser than the 808 nm laser. The results demonstrate that gold nanoparticle films are effective wavelength-selective absorbers.

2.2.2 Light Actuated Bistable Structure

Several platinum MEMS devices were created and spin-coated with GNP particles. The released bistable structures were exposed to a pulsating laser and the deflection was

measured. The device showed rapid actuation thanks to the thin film windowpanes' good thermal insulation from the substrate.

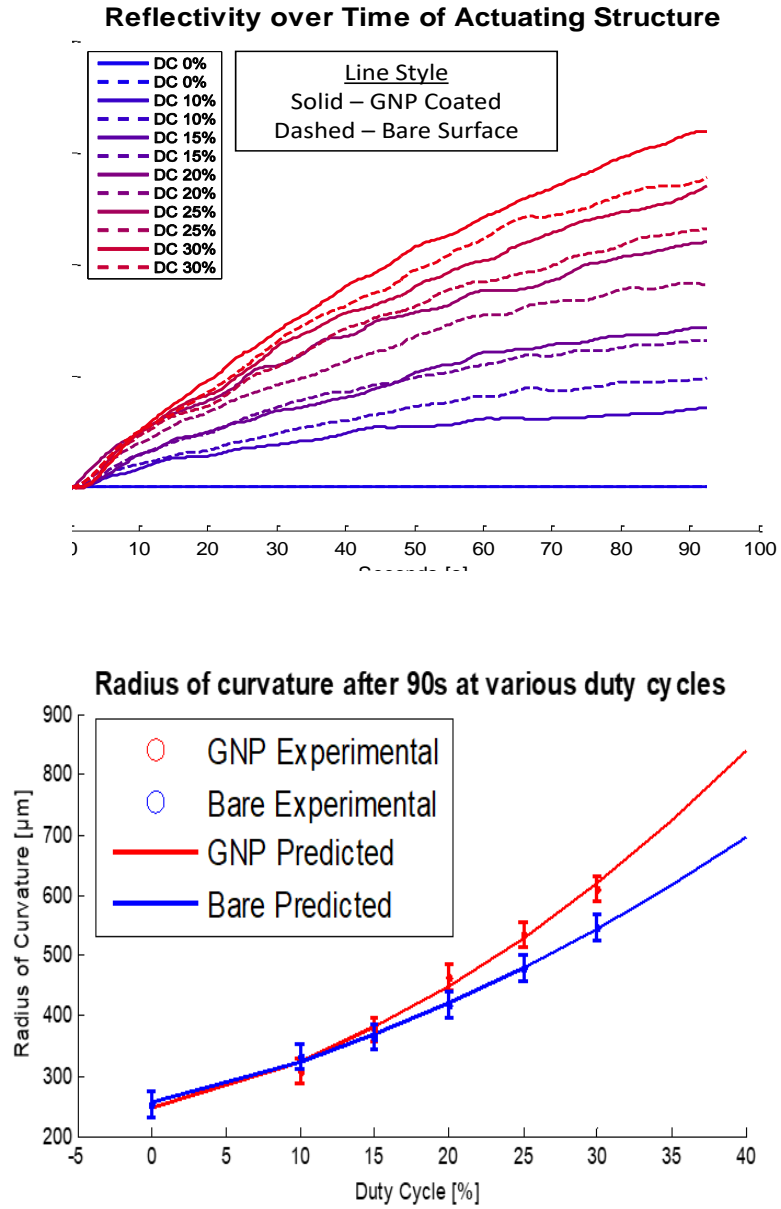


Figure 16: Windowpane device deflection under pulsating laser

Figure 16 shows the results for the windowpane actuation, and as we can see from the graph the devices which were covered with GNPs show a greater degree of change in their radius of curvature.

2.2.3 Polyimide Devices

The initial devices were platinum, and although these metal devices are easy to fabricate and useful in determining the functionality of the GNPs, they do have some drawbacks. The main drawbacks are the cost of platinum and the fact that the metal will absorb any wavelength laser to some extent. By doing so, the selectivity that GNPs provide is not fully exploited as an advantage. The cost and lack of selectivity can both be addressed by switching to a polyimide (PI) device. PI devices have been used in several MEMS applications such as flexible substrates [39], piezoelectric structures [40], and MEMS sensors [41,42].

Using PI addresses the two main drawbacks of Pt because of its low cost and the fact that it is IR transparent. In addition, PI can withstand relatively high temperatures for a polymer, has a high tensile strength, and has a linear thermal expansion coefficient of 20 ppm (parts per million) per degree C, compared to 9 ppm/C for platinum. Therefore, the PI will be able to create the necessary thermal expansion mismatch for actuation of PI/oxide bilayer structures as described in Equation 1. The IR transparency of PI allows for a novel fabrication technique where the GNPs can be placed between the PI layer and the SiO₂ layer and still provide the light selectivity. This method will be discussed in more detail in the next section.

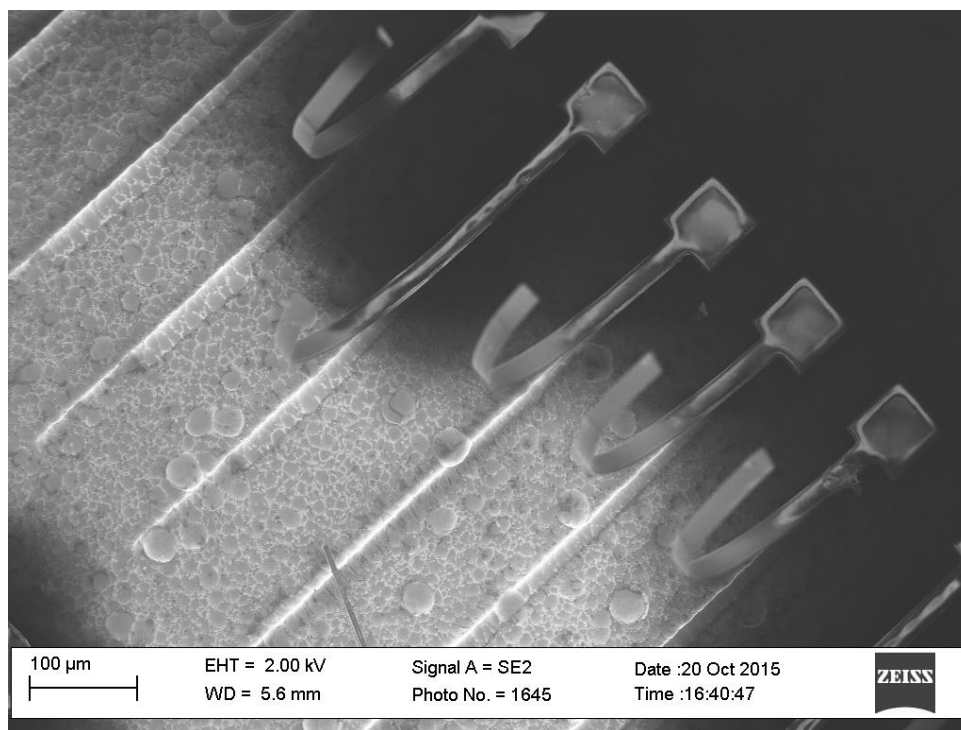


Figure 17: PI/oxide bilayer cantilevers curling up from a silicon substrate

Figure 17 shows fabricated PI devices that have been released from the wafer and curled up into a traditional cantilever shape.

2.2.4 Bulk Coating/Microfluidic GNP Patterning

In initial experiments with light actuated MEMS devices, we used metal devices with GNPs deposited on the devices post-fabrication. The deposition of GNPs after fabrication presented problems during the release because of the high selectivity of the XeF₂ etching process. This highly selective process caused the devices to release unevenly. The addition of an IR transparent polymer allowed the GNPs to be introduced during the

fabrication processes. Since the GNPs can be added during the fabrication process, a whole wafer can be covered with GNPs and then normal lithography processes can be used to create the devices. These devices have GNPs embedded in them and can be actuated using laser light. This method eliminates the problems that are present when trying to release the structures from the substrate when the GNPs have been applied after the fabrication processes.

In addition to bulk application of GNPs, using PI also allowed for the use of microfluidic devices in patterning the GNPs for a more accurate depositing process. Using microfluidic devices to pattern GNPs allowed fabrication of two devices with different wavelength GNPs within close proximity of each other on the same wafer. In addition to the proximity of the two devices, this method also allowed for the selective heating of specific segments of more complex MEMS devices. A potential application example would be precisely patterned segments on the bistable windowpane structure containing GNPs with different absorption peaks, allowing it to be switched back and forth using different wavelength lasers.

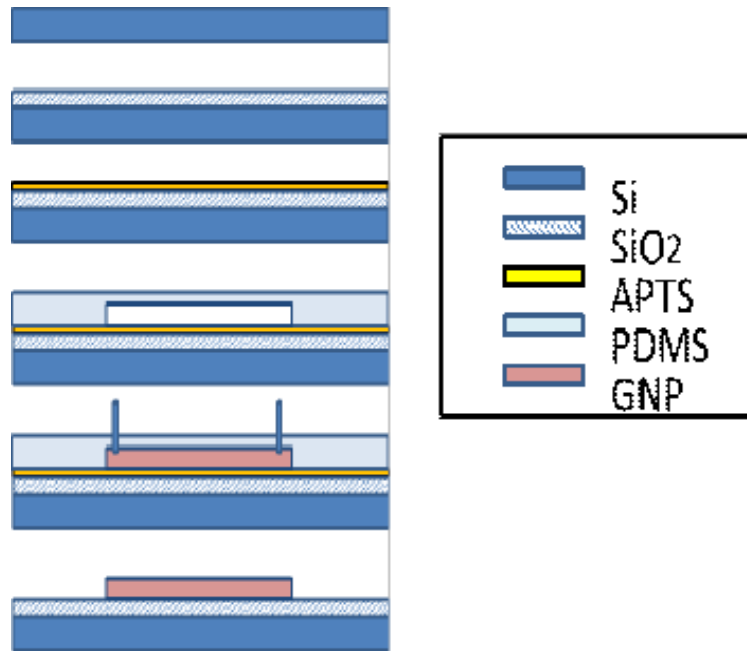


Figure 18: Fabrication diagram for microfluidic patterning of GNP devices.

The fabrication diagram in Figure 18 shows the microfluidic patterning process which was used to pattern the GNPs. The key to this process is depositing an aminopropyltriethoxysilane (APTS) layer to the surface of the wafer which helps with particle adhesion and forms a temporary bond between the wafer and the PDMS mold. The PDMS mold is bonded well enough to allow the GNPs to flow, but is easily removed after the flowing processes. Figure 19 shows the result of the patterning process before (a-d) and after (e) the polyimide is spun over the GNPs.

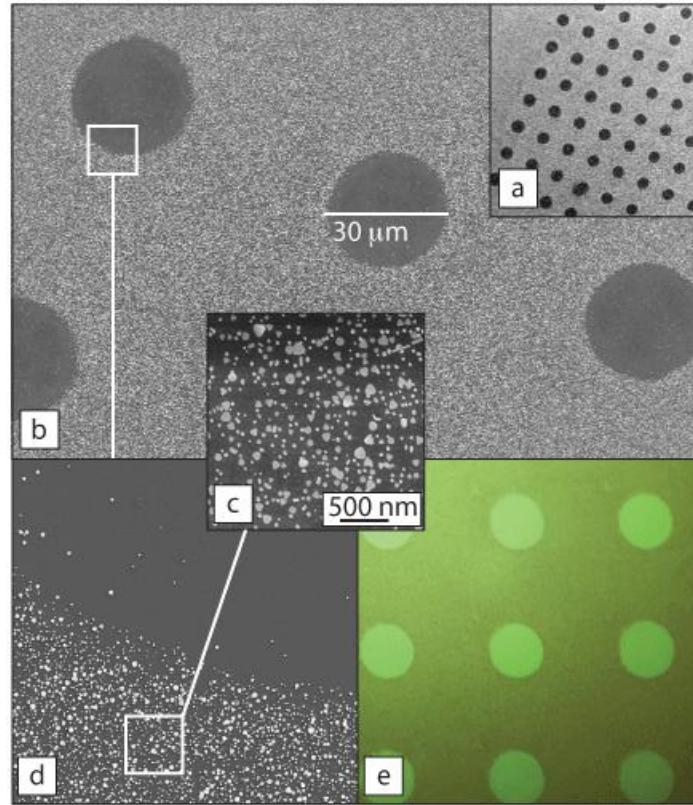


Figure 19: a - d) Scanning electron micrograph images of a GNP coating deposited onto an APTS-covered silicon surface using a microfluidic channel containing a 30 micron pillar array. e) Optical micrograph of the array after covering with a 2 micron thick polyimide film cured at 350 C.

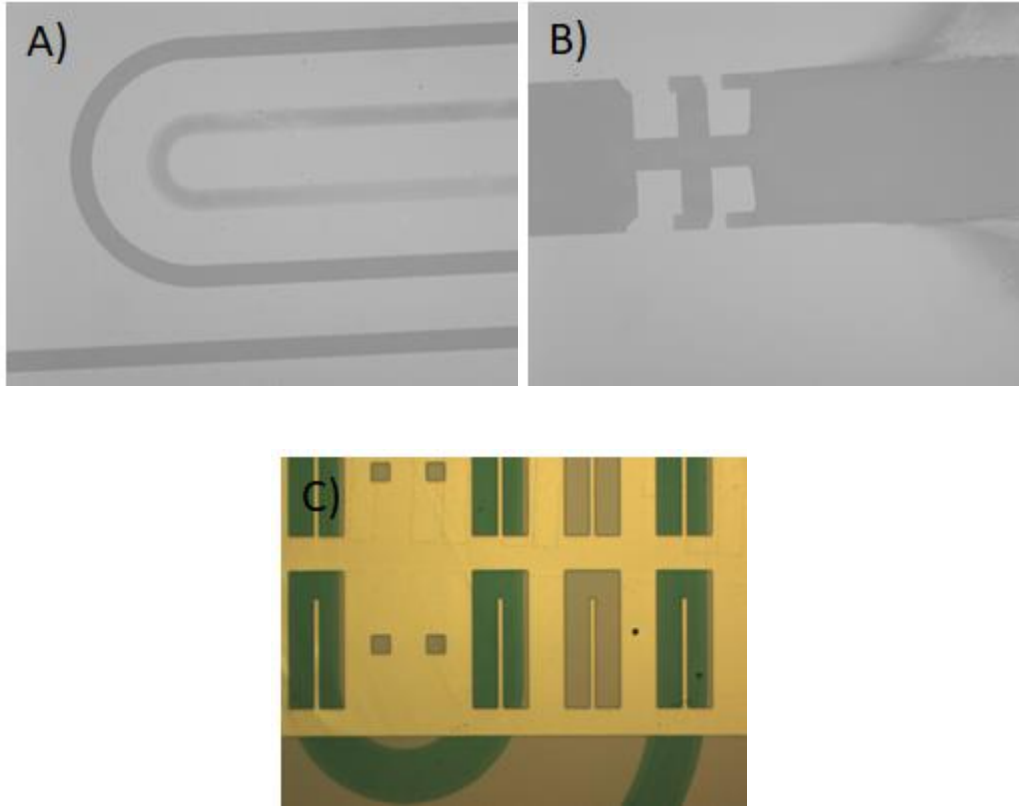


Figure 20: Microfluidic patterning GNP process A) Two different wavelength GNP patterned in close proximity to each other B) Alignment mark for photolithography C) Cantilevers aligned on top of the GNPs. The width of these cantilevers is 15 microns.

Figure 20A shows two areas of GNPs patterned in close proximity to each other. Figure 20B shows the alignment marks that are used during photolithography to align the cantilever mask. The aligned cantilevers can be seen in Figure 20C which shows three different cantilevers, the two outside cantilevers have different wavelength GNPs while the center cantilever is bare.

2.3 GNP Thermal Stability

Patterning GNPs using a microfluidic flow channel allows the GNPs to be incorporated into new devices that had not previously been possible. However, the new method exposes the GNPs to high-temperature polyimide curing processes (typically 350 C), and it turns out that these nanoparticles begin to melt at significantly lower temperatures than bulk gold (1064 C). The thermal stability of GNPs has been studied in previous research [43] showing a significant drop in the peak absorbance wavelength after heating. That research, however, was focused on nano-rod GNPs. An absorbance peak shift was also expected with the nano-plate GNPs that were used in this research, but since the plates and rods have different properties the thermal stability of the nano-rods needed to be studied and characterized further. In addition to determining the thermal stability of the GNPs for exposure to fabrication processes, thermal stability experiments were also needed to determine the safe operation parameters for these particles. As shown in the dual laser experiment, the GNPs reach a temperature of up to 80 C for a 4 watt laser. A shift in peak absorbance would affect the repeat reliability of any device which incorporated GNPs.

2.3.1 Bulk GNP Thermal Stability Experimental Setup

To measure the thermal stability of the GNPs, a monolayer of the particles was placed on several glass slides. The slides that were used were simple microscope slides that had been thoroughly cleaned, covered with APTS, and stored in 70% methanol. The APTS allows the GNPs to stick to the surface during the remainder of the experiments. The particles were placed in a circular reservoir and left to sit for two hours to ensure a uniform layer. All the slides were then measured to obtain their initial absorbance peak.

Measurements were taken at three locations along the edges of the circle and the center. The glass slides were then exposed to varying time and temperature schedules that will be detailed in the results section. The parameters were chosen based on the curing procedures of the polyimide, because this was the desired application for the GNPs. After the temperature exposure, the absorbance peak was again measured and compared to the initial absorbance peak to determine the shift due to temperature.

In addition to measuring the GNP thermal stability as a monolayer, the absorbance and particle shape of single GNPs were also measured post-temperature exposure. The particle shape was imaged using SEM and the absorbance was measured using dark field microscopy. By using unique numbered markers, we can identify individual particles and clusters of particles before and after heating. The ability to look at individual particles allows us to make determinations on the parameters which govern their thermal behavior.

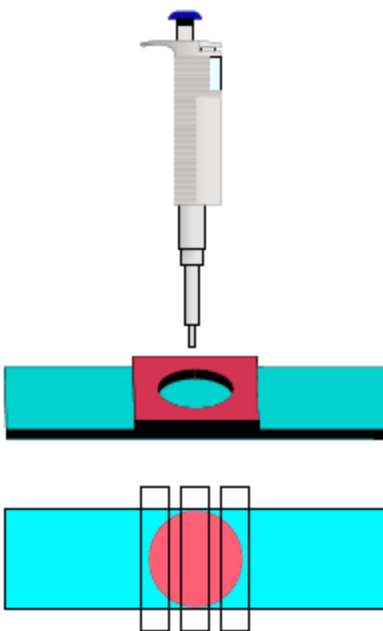


Figure 21: Bulk GNP thermal stability sample preparation and data collection locations.

Figure 21 shows the deposition method and the three locations where the measurements were taken. Data was collected at three different locations in order to minimize the effects of local variations in the bulk layer.

2.3.2 Bulk GNP Thermal Stability Results

The thermal stability experiment shows a significant shift in particle absorbance toward the smaller wavelength region of the spectrum. Although there is a significant shift in the absorbance spectrum, the GNPs do maintain a distinct peak even at higher temperatures.

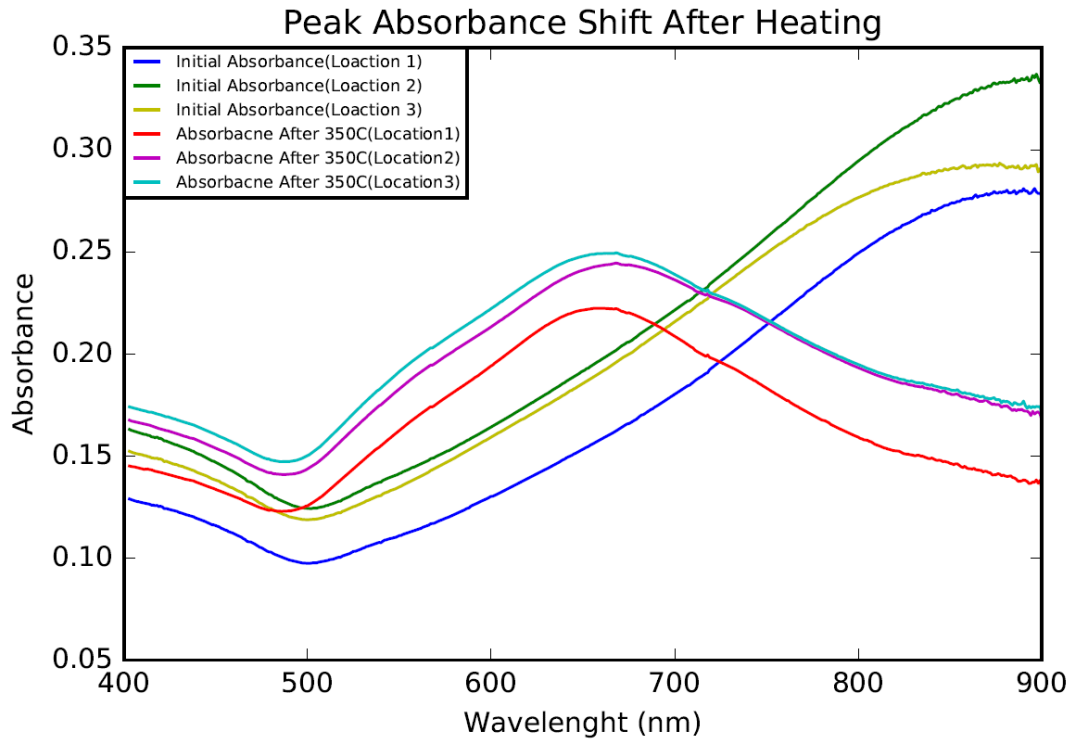


Figure 22: Absorbance profile for bulk heating experiments at 350 C.

A typical absorbance profile for bulk heating experiments can be seen in Figure 22. The figure shows the absorbance profile for three different locations on a single slide. This slide was exposed to a temperature of 350 C which is the curing temperature of the PI that was used to create the IR transparent devices.

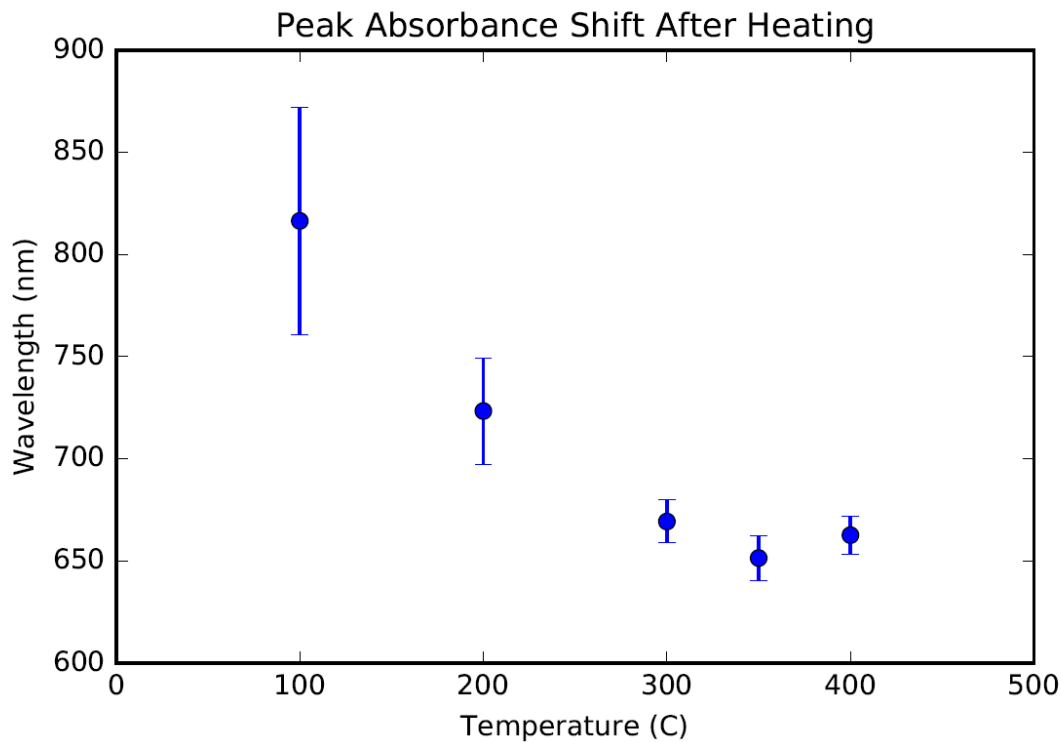


Figure 23: Average Absorbance Peak post heating

The safe region for the GNPs appears to be about 100 C. The higher region of processing temperatures from 100-400 C could still be used because the GNPs maintain a distinct peak. In addition to a shift to smaller peak wavelengths, a consistent decrease in absorbance is also observed with the bulk heating experiments. This decrease in absorbance could diminish the effectiveness of the GNPs when exposed to higher temperatures.

2.3.3 DDSCAT

The GNP absorbance as a function of wavelength was also simulated in DDSCAT, a simulation tool used to represent scattering from nanoparticle shapes that do not have an

exact solution. Unlike the spherical and rod particles, plates do not have an exact solution to determine absorbance. The GNP shapes for simulation were generated using the tools available on <https://nanoHUB.org>. The triangular geometry was generated by use of the nanoDDSCAT+ tool, which takes a shape input in the form of a mesh which is drawn in Blender software and converted to a point array, which is the input for DDSCAT [44,45,46,47,48].

The exact shape of the GNPs is difficult to determine and varies greatly, and as a result we cannot get the exact solution in DDSCAT. We can determine the general behavior of GNP triangles when the corners become rounded, evident in the SEM images. Although we cannot get an exact solution, we can determine a close approximation and a general trend in scattering from the DDSCAT simulations.

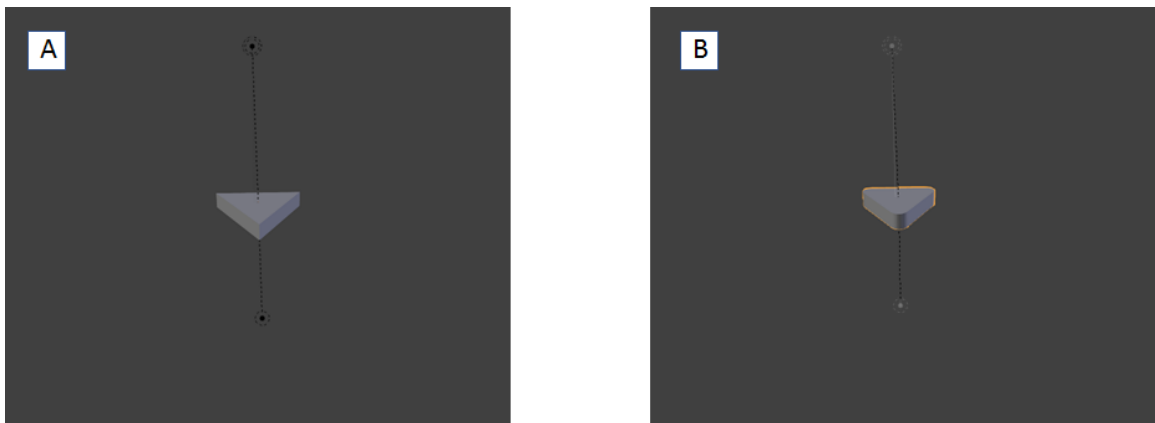


Figure 24: DDSCAT Simulation Shapes A) Triangle with sharp edges B) Triangle with rounded edges

From the simulations, we can tell that peak scattering should shift to the smaller wavelengths with heating, while also increasing the scattering efficiency. This is to be

expected because as the particles are getting rounder they are shifting to a wavelength closer to what we would see with a disk-shaped GNP plate.

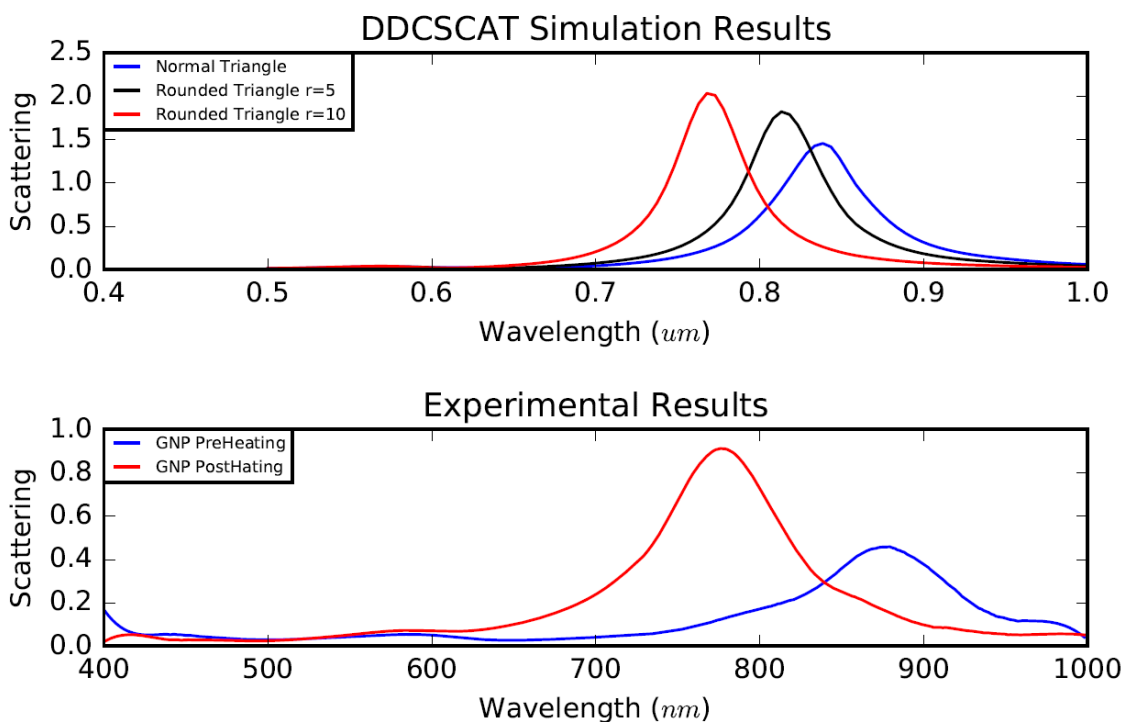


Figure 25: Experimental and simulation results for single GNP scattering

The rounded corners are created using the bevel tool in Blender. In Figure 24 the simulated results show two triangles with differently rounded corners. The rounded corners are defined by their radius in the simulations shown in Figure 25, a radius of 5 and 10 was used.

2.3.4 Single GNP Thermal Stability

To determine the thermal stability of single GNPs, a scattering profile for single particles was collected using darkfield microscopy. The scattering profiles were collected

using an Olympus scope with a cyto viva darkfield condenser. This method has been used successfully in the past to determine accurate scattering profiles for single GNPs [49,50]. A low concentration of GNPs was deposited on glass slides with unique numbered locations etched into the glass. With the help of these numbered slides it is possible to identify the same particles pre- and post- heating.

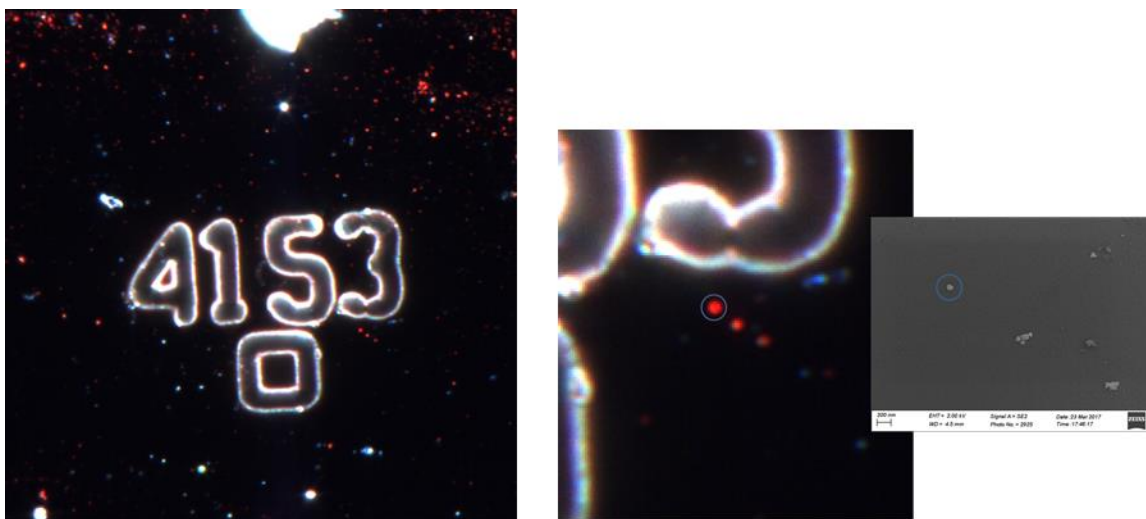


Figure 26: Method for Finding Individual GNPs using Darkfield Microscopy

Once the triangular GNPs had been identified, their scattering spectra was collected for pre- and post- heating analysis. The peak scattering wavelength was then found and a difference between the two peaks was calculated to determine the percent shift in peak wavelength. Five plates were selected for each temperature and averaged together to determine the average percent peak shift.

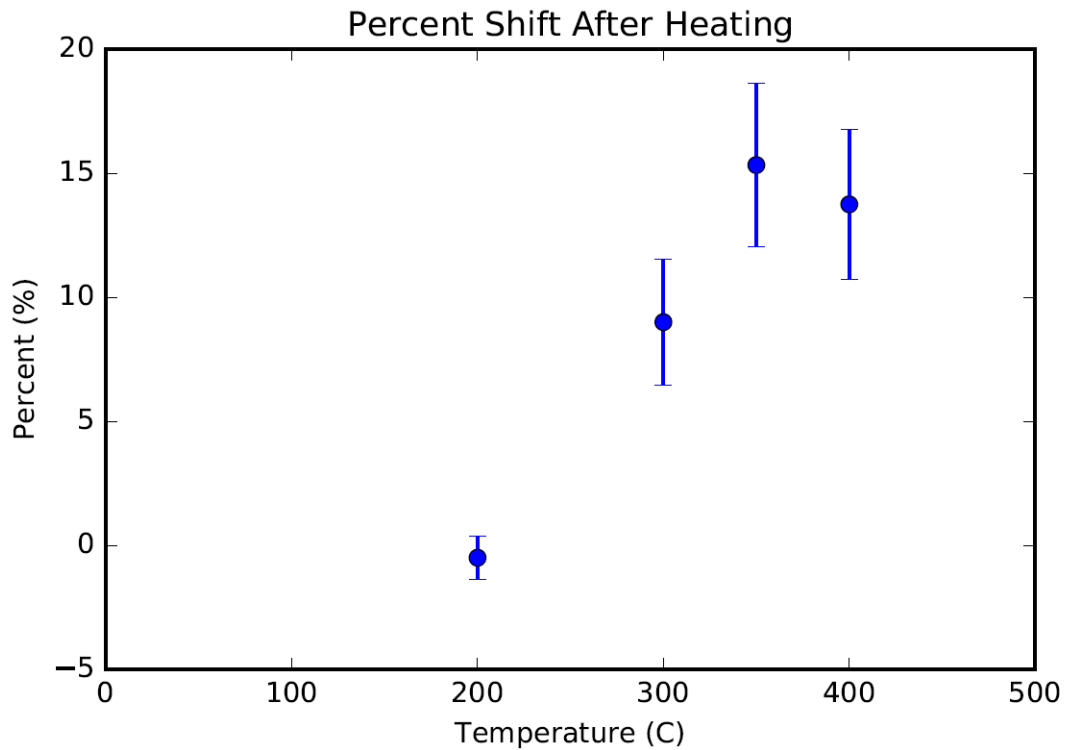


Figure 27: Single GNP percent shift for triangular particles

Similar to the bulk heating experiments in the previous section, the particles shift to the lower wavelength after heating. However, single GNPs seem to keep their original wavelength peak at a higher temperature than the bulk heating experiments show. As was mentioned in the previous section, the *bulk* GNPs show a significant shift at 200 C while in the *single* GNP experiments the shift in peak was around 0% at 200 C.

2.3.5 Thermal stability discussion

Both single and bulk thermal stability measurements have shown a significant shift in absorbance for the GNPs. The safe exposure temperature for the GNPs seems to be 100 C for bulk coating, with no to minimal shift measured at this temperature. Temperatures

above this threshold shift the maximum peak to the smaller wavelengths. This is above the temperatures we were seeing with the 4 watt laser, therefore it would be safe to assume that the absorbance of the GNPs will not change after use for the applications presented in this work. Although the GNPs would not be affected in these experiments, they could certainly be affected if a higher power laser is used. A higher power laser should be taken into account before using. The curing temperature for the polyimide used to create these structures is 350 C. This temperature has been shown to significantly change the peak absorbance of the GNPs, however, there is a commercially available PI formulation (*PI2555 DuPont*) that cures at lower temperatures near ~ 200 C [51] which could be used.

Although larger shifts have been observed with the bulk measurements, the single particle measurements have shown a smaller shift. With the bulk measurements, the GNPs have been observed to melt together and form new structures which appear to have a smaller peak absorbance. By keeping the concentration of the particles low to prevent particles from overlapping and merging when heated, higher temperatures might be safely used. However, lower GNP concentrations will lower the amount of absorbance, which may not work for certain applications such as in vivo actuation where the absorbance contrast between device and tissue must be high enough to prevent tissue damage.

Despite the fact that there is a shift in the peak absorbance wavelength, the shifted GNPs do maintain a distinct peak and therefore a lower wavelength laser could still be used to achieve thermal actuation. The peak absorbance does level off at around 650nm, which is the lower limit of the NIR window. This range would allow the melted particles to still be used for in vivo applications.

2.3.6 Light actuated cantilevers

To validate that the PI structures can be actuated, the cantilevers with GNPs embedded between the PI and SiO₂ were used. The cantilevers were placed in a SEM and imaged while a laser was fed through a vacuum flange using a fiber optic coupler. The laser was switched off (Figure 28A) and on (Figure 28B). The cantilevers can be seen deflecting in the SEM. There was rapid deflection toward the substrate, but with less amplitude than with the platinum structures in Section 2.2.2. The reduced deflection is most likely because the 915 nm laser did not overlap strongly with the thermally-shifted GNP absorbance (estimated to be in the 600-700 nm range) compared to the broad absorption band of the metal film used in the Pt cantilevers.

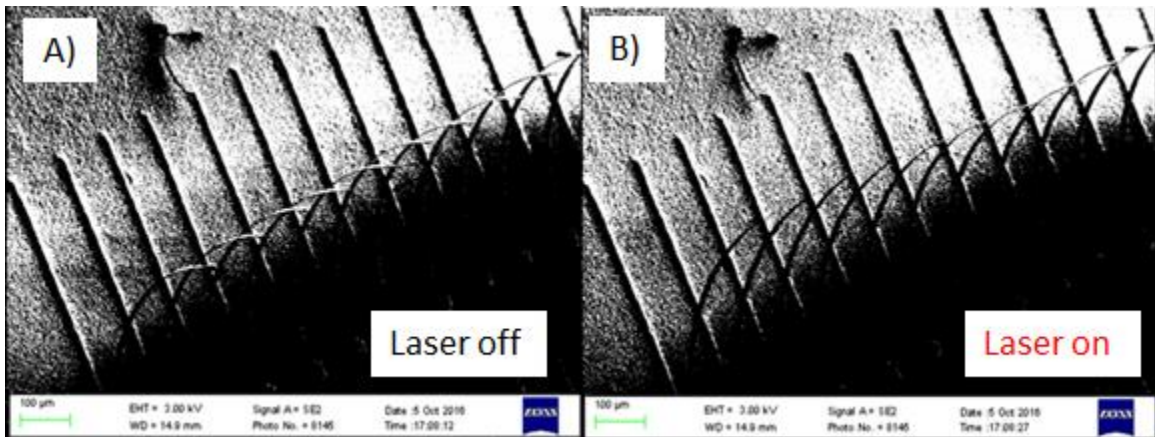


Figure 28: PI cantilevers moving under laser light A) laser off B) laser on.

The control experiment is an oxide-PI bilayer cantilever without any GNPs sandwiched between the layers. These IR-transparent oxide-PI cantilevers were not observed to actuate in the same laser spot that caused observable motion in oxide-GNP-PI cantilevers. Figure 29 shows the side-by-side GNP/control cantilever arrays with the laser

off (A), and on (B). This result illustrates the success of using PI instead of platinum as the thermally expanding material for laser-induced microactuation. Although PI introduces some fabrication challenges related to melting and wavelength-shifting in the GNPs, it creates better thermal contrast between GNP and non-GNP coated areas.

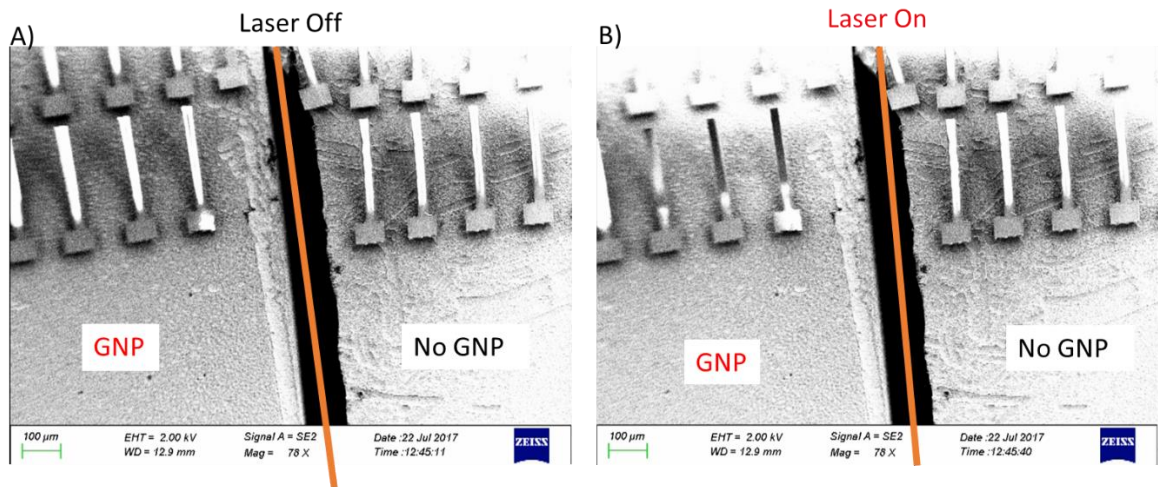


Figure 29: Side-by-side GNP/control cantilever arrays

CHAPTER III: INDUCED CHARGE ELECTRO-OSMOSIS

In this chapter, we apply an external electric field to metallic nanostructures not as a laser beam, but as an AC electric field at a pair of electrodes in a microfluidic cell. Like the GNPs in the previous section, the metallized structures here are electrically floating and able to respond to the external field by polarizing and acquiring a non-uniform surface charge. The chief application investigated in this part of the thesis is driving fluid through a metal-lined nanopore using the induced surface charge to perform electroosmosis.

3.1 ICEO Background

The induced-charge electroosmotic (ICEO) effect occurs when a conductor is placed in a liquid medium and an electric field is applied, which causes the conductor to become polarized. Since the conductor has to maintain a zero-net charge, the conductor gains a non-uniform surface charge distribution. The positive and negative charges on the conductor then attract counter charges in the fluid. The applied electric field prompts the free ions to move which causes the counter-ions in the fluid to also move. This movement in the fluid creates vortices which drag the rest of the fluid to create continuous flow.

3.2 ACEO Background

A subset of electroosmotic flow is Alternating Current Electro-Osmosis (ACEO); these devices use an AC voltage to induce flow. When an AC voltage is applied, it does not generate the electrolysis gas bubbles that can break the circuit of a direct current (DC) electroosmotic pump. For this practical reason, AC-driven induced charge electroosmosis (ICEO) around polarized metal obstacles in flow channels has been an active research topic for more than a decade. Net flow is allowed even in symmetric AC fields thanks to asymmetric features in microfluidic channels. The Helmholtz-Smoluchowski slip velocity u_s in a DC field is given by Equation 11.

$$u_s = \frac{\varepsilon\zeta E_{||}}{\eta} \quad (11)$$

Where η is the electrolyte viscosity, $E_{||}$ is the tangential component of the applied electric field, ε is the permittivity, and ζ is the zeta potential of the surface [52]. The first ACEO pumps used symmetrical planar electrodes to obtain flow [53].

3.3 Obstacle ICEO/ACEO

In microfluidic ICEO, the central object in experiments or simulations is typically a conductive floor-to-ceiling obstacle in a microfluidic channel. In these experiments flow is horizontal, which is excellent for video microscopy and capturing streamlines using fluorescent tracer particles that stay within the microscope's focal plane for good frame-

to-frame correlation. Figure 30 shows examples of this type of research from our previous work.

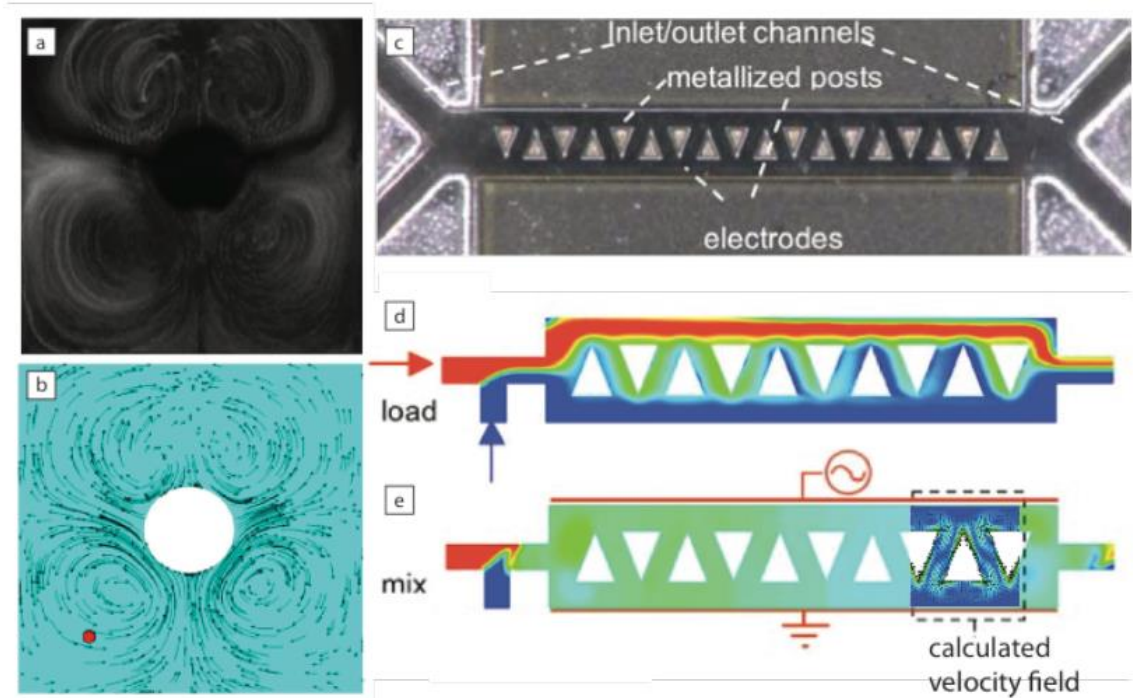


Figure 30: Images taken from our previous work [54] with flow in the plane of the page. (a) Fluorescent tracer beads moving around a polarized circular pillar are turned into flow streamlines (b) using particle image velocimetry. (c) Asymmetric metal-coated triangular pillars (channel width 200 microns and depths of 50-300 microns), (d), their simulated loading, and (e) continuous mixing of two flowing solutions in a transverse AC electric field by both ICEO and diffusion.

Induced charge electroosmosis ion current rectification in nanopores and nanotubes with broken symmetry is defined by etching a two-dimensional pattern, and then laminating different layers together. Micro- and nanopores do not integrate readily into this fabrication process or into experiments involving video microscopy. Pores can be

integrated into a microfluidic device by sandwiching a porous membrane between two channels [55], or by packing a channel with a polymer monolith that forms pores by self-assembly [56]. However, these unconventional materials bring the fabrication sequence outside the cleanroom, and both methods create flow streamlines that move out of the focal plane. Investigating ICEO in a porous format calls for an upgrade to the microfabrication toolbox and a 90° rotation of the flow direction.

3.3 Applications of ICEO at membranes

Motivations include compact lab-on-a-chip systems that require higher backpressure than can be achieved with microscale pumping features, and compact hydraulic systems for robotics.

3.3.1 Lab-on-a-chip

A lab-on-a-chip (LOC) is described as a device that integrates one or more laboratory functions on a single integrated device on a small scale, generally on the millimeter scale [57]. One of the advantages of LOCs is that they can handle relatively small fluid volumes down to less than pico liters. LOCs still rely on external pumps or pressure driven flows [58] which limits their portability and increases their size. The small fluid volumes and reliance on bulky pumps make LOCs an attractive application for ICEO pump.

3.3.2 Soft Robotics

Soft robotics requires fluid pumps that can attain 10-100 psi, with as few moving parts and exotic materials as possible. Hydraulics [59] and pneumatics [60] are in the right range to power state-of-the-art soft actuators. However, the actuation of these soft robots is usually created with a conventional pump or even a high-pressure gas cylinder and regulator that remains off-camera during demonstrations. The main selling point of soft robots is their flexibility, and having rigid components like a pump or gas cylinder reduces such benefits. Since the membranes presented in this project are flexible and thin they would be a significant addition for soft robotic applications.

3.3.3 A gap in the literature

There is a lack of cross-talk in the literature between microfluidics groups carrying out horizontal flow microfluidics experiments, and membrane and nanopore groups that use a flow-through geometry. By taking an existing microscale phenomenon to the nanoscale, we aim to link the ongoing efforts of both groups of researchers. Microfluidic ICEO research produced a surge of papers between 2004-2010 that focused on fluid dynamics, simulation, surface chemistry, and applications in lab-on-a-chip fluid transport at the microscale. Meanwhile, another rich and innovative research field developed around ion transport in conical nanopores; that work is often motivated by single molecule detection.

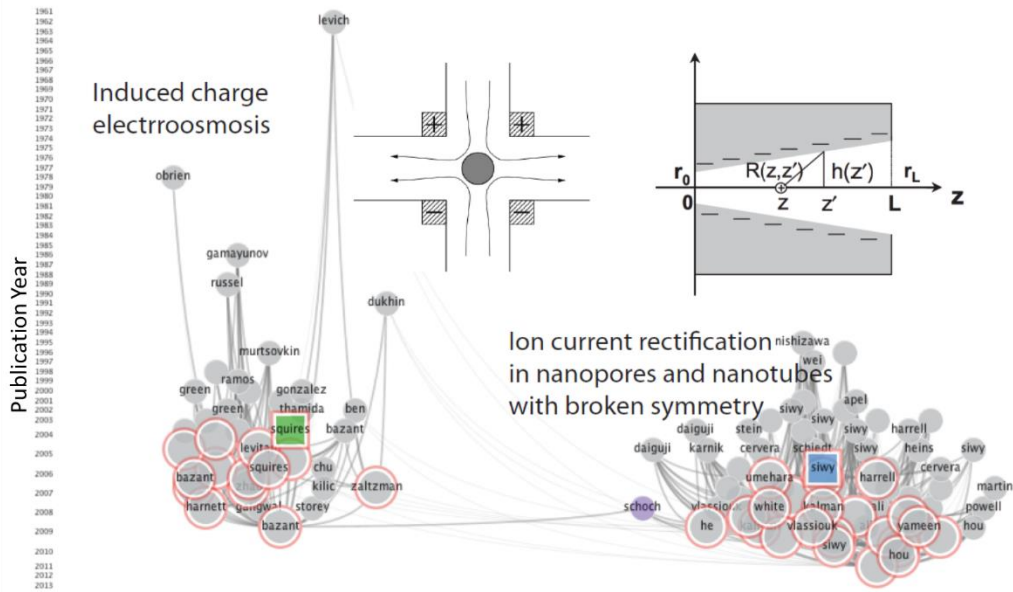


Figure 31: Research on induced charge electroosmosis (ICEO, left) and on ion flow through nanopores (right) investigates related phenomena, yet there is little cross-referencing (indicated by lines connecting gray circles) between two key papers (green square, blue square) on these topics.

In Figure 31, an early ICEO paper by Squires and Bazant [61] became the most heavily cited paper in the Journal of Fluid Mechanics; this paper suggested that the microfluidics community should apply metal to obstacles in channels with in-plane flow. A couple of years later, a key paper by Siwy on ion-current rectification in nanopores [62] described experiments with a flow-through geometry, and had connections to groups that metalize the inner wall of nanopores using electroless plating [63]. Gray circles are works that cite either Squires or Siwy directly (red ring), plus the other papers in their bibliography. As of fall 2016, the shortest link between the two bodies of literature is still a massive review paper on nanofluidics by Schoch [64]. Currently, few crossovers are seen

between these two fields, but the groups are poised to make an impact by combining their expertise. Nanomaterials researchers have new tools and techniques that can apply the fast, AC-generated slip velocities of ICEO over a much larger surface area than previously possible. Linking these two topics together through this collaborative proposal has the potential to generate high pressure unidirectional flows in high ionic strength solutions, using AC electric fields that mitigate the problem of electrolysis bubbles. Cross-collaboration will combine the controllable surface charge density of ICEO with the understanding of ion distribution at the small dimensions investigated by the nanopore research community.

CHAPTER IV:
ALTERNATING CURRENT ELECTRO-OSMOTIC PUMPING AT
ASYMMETRICALLY METALLIZED POROUS MEMBRANES

The goal of this section is to investigate AC electro-osmotic pumping through asymmetrically metallized membrane nanopores for bubble-free, electrically driven fluid transport in compact lab-on-a-chip systems that require higher backpressure than can be achieved with microscale pumping features [65]. Induced charge electroosmosis (ICEO) is able to drive flows at conductive surfaces that persist even in alternating current (AC) electric fields [66]. Because previous work in this area uses microfabricated pillars as discussed in the previous section, the flow-through format described here is a departure from past work in the field. We have created several types of metallized membranes and tested them under different conditions. To validate our experimental results and to optimize our parameters we have also performed computational fluid dynamics (CFD) simulations. The work is motivated by the idea that nanoscale pore geometry can potentially exceed the pressure limitations of current ICEO and alternating current electroosmosis (ACEO) microscale systems. Nanoporous materials made either by self-assembly, or by “top-down” nanolithography, will open the possibility of using ICEO in new applications including lab-on-a-chip sample preparation. With this project, we hope to accomplish several goals:

1. Create a scalable fabrication technique for single sided metalized membranes for use in an ICEO device.
2. Determine fabrication limitations
3. Verify ICEO flow through metalized membranes
4. Determine optimal operating parameters for these metalized membranes

4.1 Flow-through ICEO Background

In this section, we present a flow-through approach to induced charge electro-osmotic pumping, by using single-sided metallized nanoporous membranes for alternating-current (AC) driven fluid transport. ICEO devices have not yet been created at the scale of the Debye layer thickness, which increases to 100 nm with decreasing salt concentration. Consequently, their active pumping area is only a small fraction of the device volume, and their relatively large channel size means they are unable to hold off significant pressures. In this work, we have investigated the ICEO principle at a nanoporous membrane surface, where instead of metal obstacles in a microfluidic channel, there are metal-lined pores with sub-micron diameters.

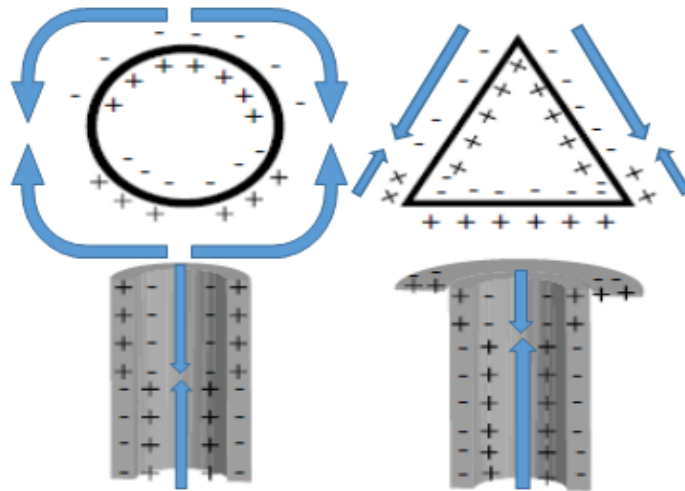


Figure 32: Illustrates how asymmetry (right side) can drive nonzero flow around an obstacle or through a pore in an AC trans-membrane electric field. Top row: Typical flow around obstacles designed for horizontal microfluidic flow; asymmetry is achieved by applying a metal coating to an asymmetrically shaped obstacle. Bottom row: The same concept applied to vertically-polarized pores for through-substrate flow; asymmetry is achieved by applying metal to one side of a porous membrane.

The polarized metal film maintains zero net charge, but the externally applied electric field induces a non-uniform surface charge. This surface charge attracts counterions, forming a double layer at the surface. The external electric field drives the ions in the double layer with a slip velocity that creates bulk flow through the pore. Because of asymmetry (Figure 32, right side) the induced flows need not cancel out as they would with a symmetric structure (Figure 32, left side). With the asymmetric geometry of the metallized pore, the time-averaged ICEO flow moves in a single direction -- toward the

metallized surface -- even in alternating current (AC) electric fields, as long as the frequency is low enough to allow the double layer to form.

In this project, we have created metallized membranes by photolithography and by sputtering gold on track-etched nanoporous membranes. We then tested their pressures and flow rates under different conditions. To validate our experimental results and to optimize our parameters we have also performed computational fluid dynamics (CFD) simulations. The work is motivated by the idea that nanoscale pore geometry can potentially exceed the pressure limitations of current ICEO and (ACEO) microscale systems. Nanoporous materials made either by self-assembly, or by “top-down” nanolithography, will open the possibility of using ICEO in new applications including lab-on-a-chip sample preparation.

A significant amount of research has already been devoted to the development of microfluidic pumps in applications such as filtration, medical diagnostics, and separation. Advances in electronically driven pumping are needed in order to reduce the size and cost of these devices.

4.2 ICEO Device

4.2.1 Fabrication

We have produced flow-through ICEO structures using both top-down photolithography for optical microscopy experiments, and track-etched nanoporous polymer membranes for pressure measurements. Unlike traditional micropillar-based ICEO devices, the fabrication of these asymmetrically metallized membranes is a simple process. Nanoporous ICEO structures are fabricated by sputtering gold onto off-the-shelf track-etched nanoporous polycarbonate membranes. The sputtering process coats only the top and side walls of the membrane, breaking the symmetry of the metal coating. Track-etched pores are commercially available at nanoscale diameters (80 nm- 1 μm) which are not achievable using photolithography. Although the track-etched membranes provide nanoscale features for backpressure generation, their random distribution and small size makes it difficult to optically image the flow pattern at individual pores. Therefore, larger and more uniform pores are needed for optical studies. These larger pores were created using SU-8 epoxy-based photoresist and standard cleanroom lithography processes. The membranes were created by first depositing a sacrificial layer of styrene onto a wafer, followed by standard SU-8 lithography and release in toluene. The released SU-8 membranes were transferred to a silicone carrier and metallized by sputtering as detailed in Figure 33.

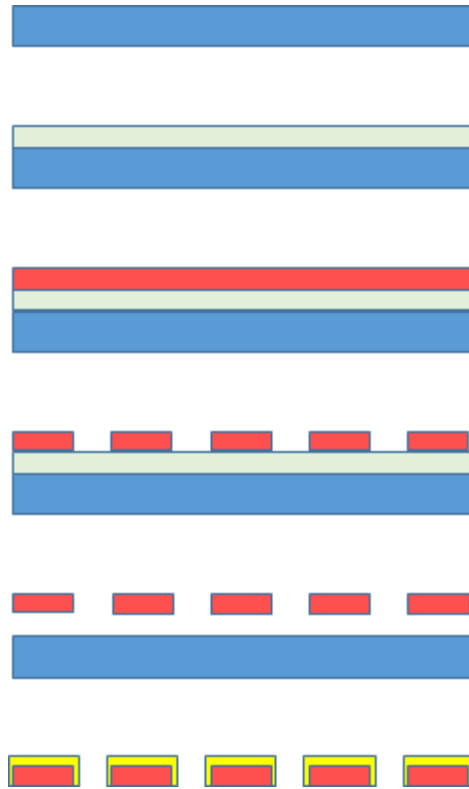


Figure 33: Fabrication Diagram for ICEO Membranes

4.2.2 Fabrication Limitations/Characterization

To better understand the behavior of the membranes and to refine our simulations, the membranes were visually characterized using SEM and optical microscopy. The sputtering process is a repeatable and scalable method for producing the metalized membranes, but there are some limitations that arise from using this method. The biggest limitation to this process is the pore diameter of the membranes. Once the pores have been sputtered they are analyzed using the SEM (Figure 34) to verify that the pores are not clogged. Several membrane sizes have been sputtered including 100 nm, 200 nm, 400 nm, 600 nm, 800 nm, 1000 nm, and 3000 nm. The smallest membranes that have been created

successfully have been the 400 nm membranes; membranes below this threshold have been clogged. The reason for the clogging is not known, one possibility could be that at smaller pore sizes the gold deposition process is able to form a bridge across the membrane. The reason for clogging needs to be investigated further.

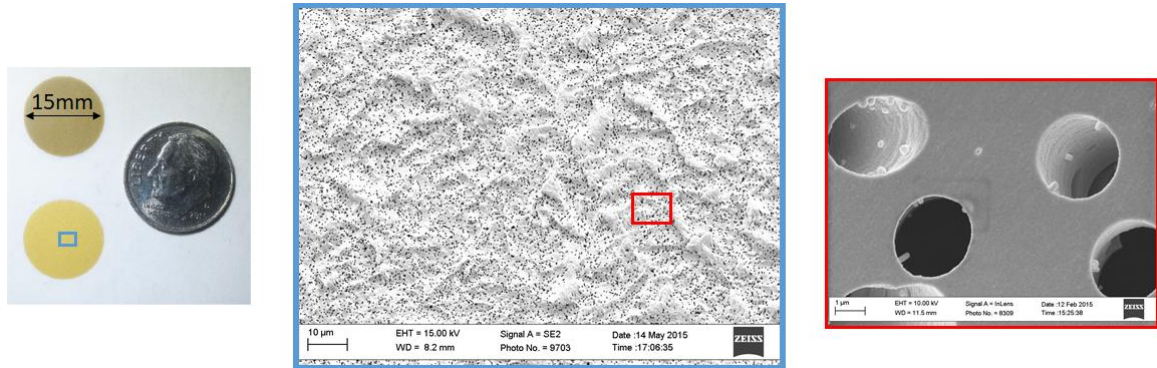


Figure 34: Asymmetrically metallized nanopores fabricated by metallizing track-etched membranes

In addition to determining if the membrane pores are open, the membrane sidewalls were also imaged to determine how much was covered. The cross-sectional view in Figure 35 shows the gold covering the side of the wall about halfway down.

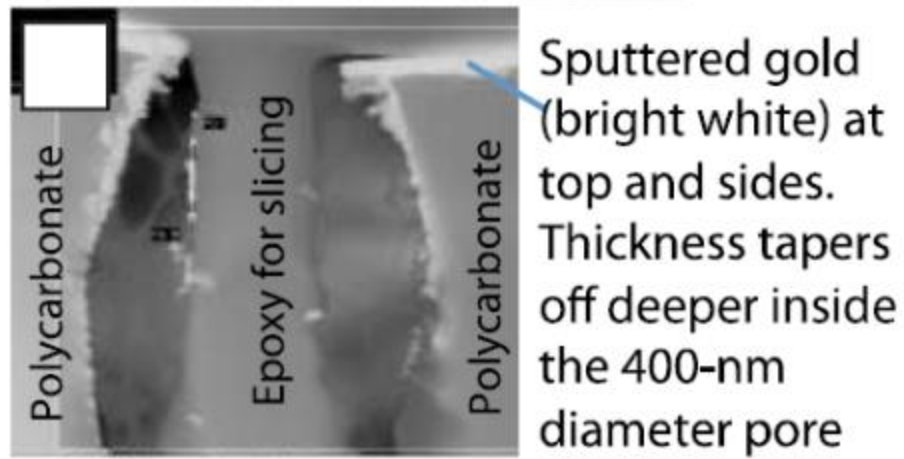


Figure 35: Cross sectional view of a membranes showing gold deposited along the side walls

This cross-sectional view shows that there is the desired asymmetry present in these devices which is needed to achieve ACEO flow.

4.3 Experimental Results

4.3.1 Theoretical Expectations

There are several parameters which have an effect on ICEO flows. In order to validate the presence of the ICEO effect and to better understand the behavior of the devices, multiple variables have been tested.

1. Varying the voltage applied across the device

We expect the pressure and flow velocity to increase with increases in voltage. We expect this because increasing the voltage will increase the electric field, which will increase both the induced charge and the electrophoretic force acting on it. The applied voltage from the system was varied between 30 -150 V_{rms}. Although the applied voltage is very large, the voltage across the membrane is in the 1 V range due to the high impedance created by the testing device which can be seen in Figure 36.

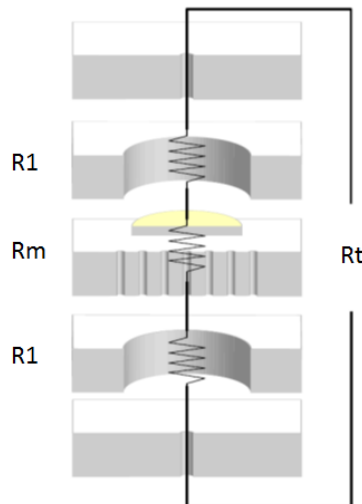


Figure 36: Impedance calculations for obtaining voltage across membrane

This low voltage across the membrane indicates that the voltage needed to drive the system could be much smaller if the electrodes were closer together.

2. Varying the frequency

a. Higher driving frequencies (> 1000 Hz) quenched the ICEO effect. The effect will continue to appear as long as the induced-charge screening cloud has sufficient time to form. Based on our previous projects [67] and the literature [68], a frequency between 200 Hz and 1 kHz seems to be the ideal operating parameter.

3. Varying the conductivity in the medium

We expect the increased conductivity in the medium will decrease the ICEO effect, because several experimental results have shown a decrease in efficiency when it comes to an increase in ionic strength. There is about a 75% drop in velocity when going from a solution with .001 mM to 1.0 mM [69]. Although the standard model does not seem to be able to accurately predict the effects of a high ionic strength solution, there have been attempts made to add to the standard model in order to account for this. One such approach uses direct numerical simulations of the coupled Poisson-Nernst-Planck equations and the Navier-Stokes equations which show that there is a chaotic flow phenomenon present [70]. The simulations that were presented show that with a high ionic strength solution, a dense collection of ions can form and conduct a sufficient amount of current to effectively short out the metal surface and therefore diminish the ICEO effect.

4. Varying pore diameter

We expect the pressure output of the device to increase with smaller pore size devices because the smaller pore diameter can withstand significantly larger backpressure. According to our numerical calculations (described further in Section 4.3.2) we expect the pressure to increase with the decrease in pore diameter as seen in Figure 37. We tested membranes from .4 μm to 3 μm ; this size scale was chosen because we are not able to fabricate devices below .4 μm with our current fabrication techniques. The upper limit of 3 μm was chosen because the pressure sensor which is being used cannot sense sub- 20 Pa pressures which are produced by pores larger than 3 μm .

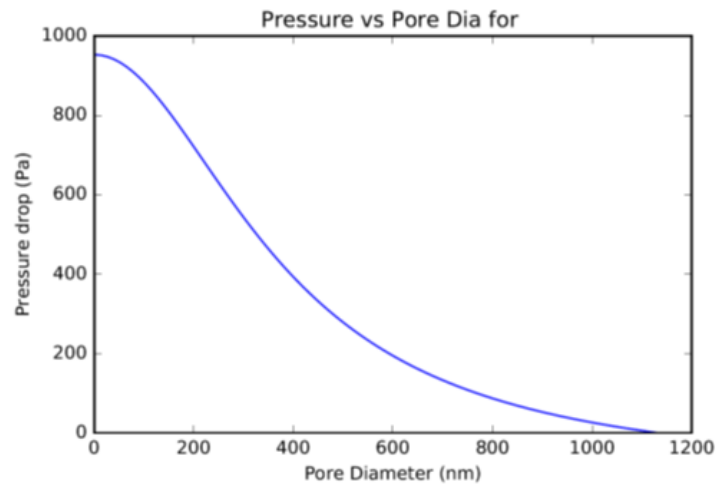


Figure 37: Expected pressure output vs pore diameter

5. Control Experiments

Two different control groups were used to determine if the metallization was responsible for the pressure and flow effects. The experiments were performed with a non-metallized pore placed in the testing setup. In addition to this, the experiment was also

performed with no membrane present in the setup. Although achieving flow in membranes is possible with non-metallized membranes in AC fields [71], non-conductive membranes need asymmetric shapes (such as tapering pores) to produce pressure. The control experiments were expected to not produce any pressure change because there is no asymmetry with the non-metallic track-etched membranes used in this project.

4.3.2 Numerical Calculations

To calculate the pressure output, the Helmholtz-Smoluchowski slip velocity Equation (11) can be used since ICEO velocity remains the same under AC fields however the equation does need to be modified as presented in the literature [72]. Since only the induced potential contributes to the time-averaged flow, the equation reduces down to Equation (12) where a is the polarized surface length.

$$u_{ICEO} = \frac{\varepsilon E^2 a}{\eta} \quad (12)$$

The pressure of these systems can be calculated by first obtaining the volumetric flow Q from Equation (13).

$$Q_{max} = A \frac{\varepsilon E \zeta}{\eta} \quad (13)$$

A is the cross-sectional area of the structure. The pressure generated by the structure can be calculated by assuming that the ends are capped. To satisfy the conservation of mass, an equal and opposite flow is required; this pressure driven backflow is given by

Poiseuille flow as shown in Equation 14 where L is the channel length and s is the smallest cross-sectional dimension.

$$Q_p = A \frac{\Delta P s^2}{\eta L} \quad (14)$$

In setting the two equations equal to each other, we obtain the maximum pressure change (ΔP) plotted as the red dashed line in Figure 38.

$$\Delta P_{max} = \frac{\varepsilon E \zeta L}{s^2} \quad (15)$$

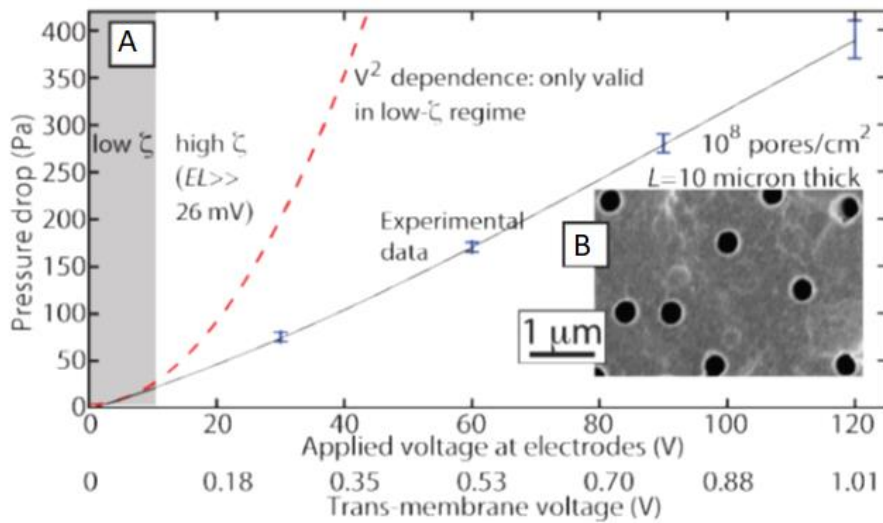


Figure 38: (A) Pressure-vs-voltage is nearly linear (B) Electron micrograph of membrane.

Equation 15 has been used as the basis for ACEO pumps in porous structures with lateral flow [73,74]. However, the data in Figure 38 (black line) shows the pressure diverging from the V^2 dependence predicted in Equation 15. This discrepancy is consistent

with our previous results on ICEO devices [75] and with most reports in the literature. The V^2 scaling only holds true for low ζ potentials but diverges in the high ζ potential region. This departure has been attributed to many factors such as ion crowding. To account for this divergence, correction factors are generally introduced [76]. The correction factor A is the ratio between the theoretical and measured results.

4.4 Measurements

Pressure measurements were performed with a MPXV7002DP pressure sensor which outputs a voltage proportional to the pressure difference across the membrane. The voltage was collected using LabVIEW and analyzed in Python.

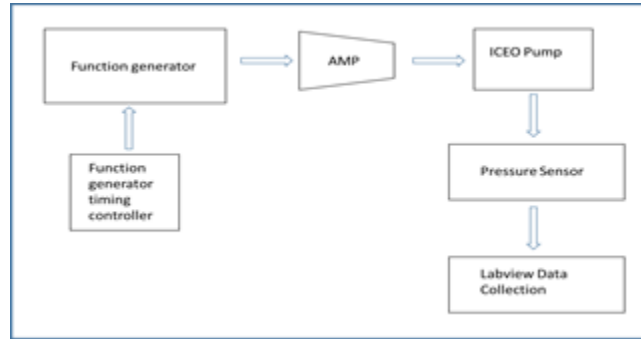


Figure 39: Block diagram for data collection

The pressure measurement device consisted of a membrane sandwiched between several acrylic laser-cut pieces which function as scaffolding to hold the membrane in place and as reservoirs for the flow medium. Two stainless steel tubes serve as connectors to the pressure sensor and as the positive and negative electrodes for the voltage. A breakdown of the testing device can be seen in Figure 40.

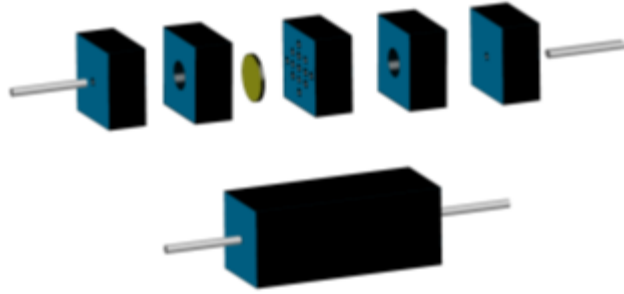


Figure 40: Laser cut acrylic pressure measuring device

To validate that we were seeing ICEO flow, we created larger membranes using SU-8. These membranes were large enough to observe flow behavior. Electrical contact was made using platinum wires immersed in the reservoirs. The membrane was placed above one end of the connecting channel. By using an indium tin oxide slide as a transparent electrode and substrate for the microfluidic channel, the membrane could be polarized while tracer particles were observed using inverted fluorescence microscopy. The flow was recorded using an INFINITY3-3ur video camera.



Figure 41: Flow Visualization Device: A membrane polarized between a wire and an optically-transparent conductive indium tin oxide coated slide is inspected in an inverted optical microscope during operation.

4.4.1 Simulations

Simulations were performed in ANSYS Fluent CFD software to determine if a pressure difference could be created in metallized pores. A moving wall in an axisymmetric domain was used to create electroosmotic slip along the pore walls. The wall velocity was non-uniform and was computed as follows. The surface charge density along the wall was calculated using ANSYS Maxwell. The resulting charge density distribution was then imported into the ANSYS Fluent mode to calculate flow velocity vectors. The goal was to determine the net flow, which combines ICEO-driven flow with pressure-driven backflow and the maximum pressure and flow rates attained by a given geometry. Maximum velocity was calculated by leaving the inlet and outlet open. Using these simulations allows us to determine the optimal parameters to enhance our device performance.

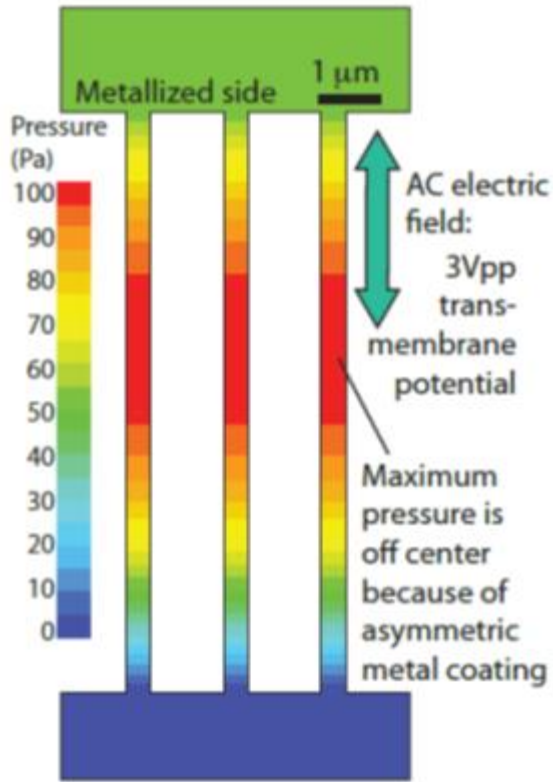


Figure 42: Simulation Visualizations and differential pressure validation

The simulation results in Figure 42 are derived by applying a moving wall velocity on the side walls which creates a pressure difference between the inlet and outlet.

4.4.2 Pressure Measurement Results

Out-of-plane tracer particle motions were observed during fluorescence microscopy of active pores in AC electric fields. Pressure measurements depended on several variables.

Increasing the voltage (0-120 V_{rms}) resulted in an increase in pressure, with typical maximum pressures in the 400 Pa range for a single membrane and higher for stacked

membranes. The pressure increased linearly with the increase in voltage to about 120 V_{rms} and then leveled off to only a modest increase.

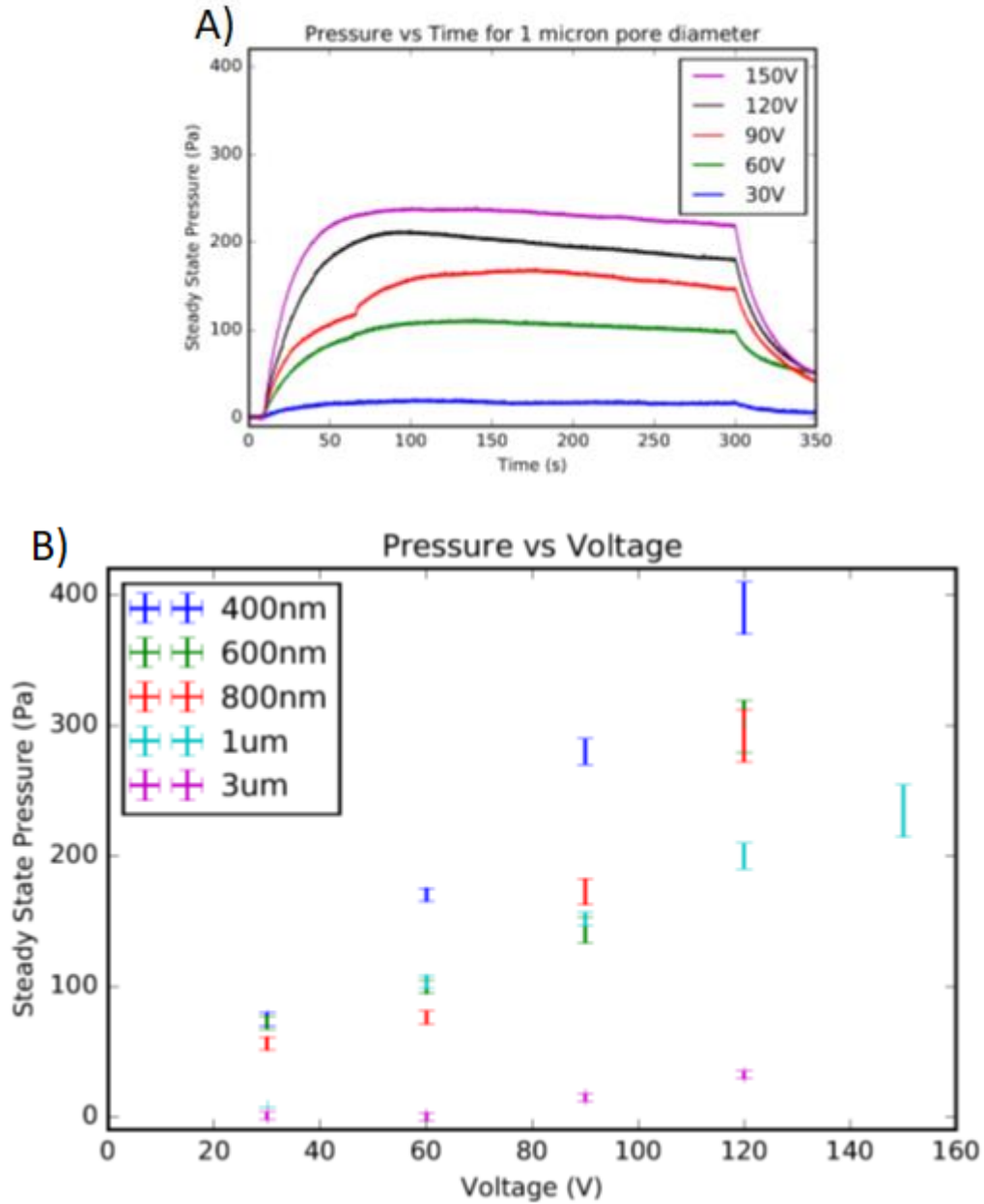


Figure 43: Device Voltage Response A) Typical voltage-vs-time response for membranes with 1 micron pore diameters B) Steady-state Pressure vs Voltage for membranes with different pore diameters

A typical pressure response for different voltages can be seen in Figure 43A. The steady state pressure shown in the graph takes a few seconds to build up. This is due to the fact that when an incompressible fluid is in a flexible wall there is a large compliance, and the pressure causes the tube to expand and increases the volume available to the water. In addition to the tube being able to expand, bubbles also have a large compliance although steps have been taken to eliminate this. Small bubbles could still remain in the device, which would also effect the time to reach steady state.

Higher driving frequencies (> 1000 Hz) quenched the ICEO effect as the ions in the fluid could not diffuse fast enough to respond to charges on the metal surface. The experimental results shown in Figure 44 were collected by switching between 400 Hz and from 1000 Hz-3000 Hz.

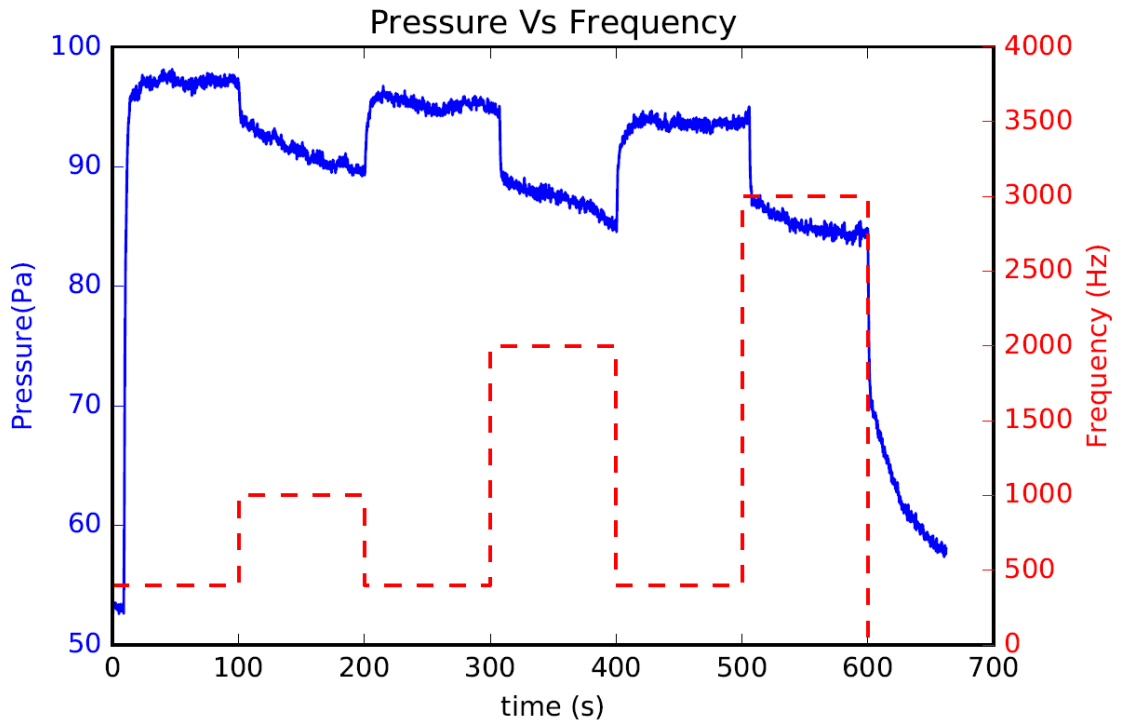


Figure 44: Pressure response to change in frequency

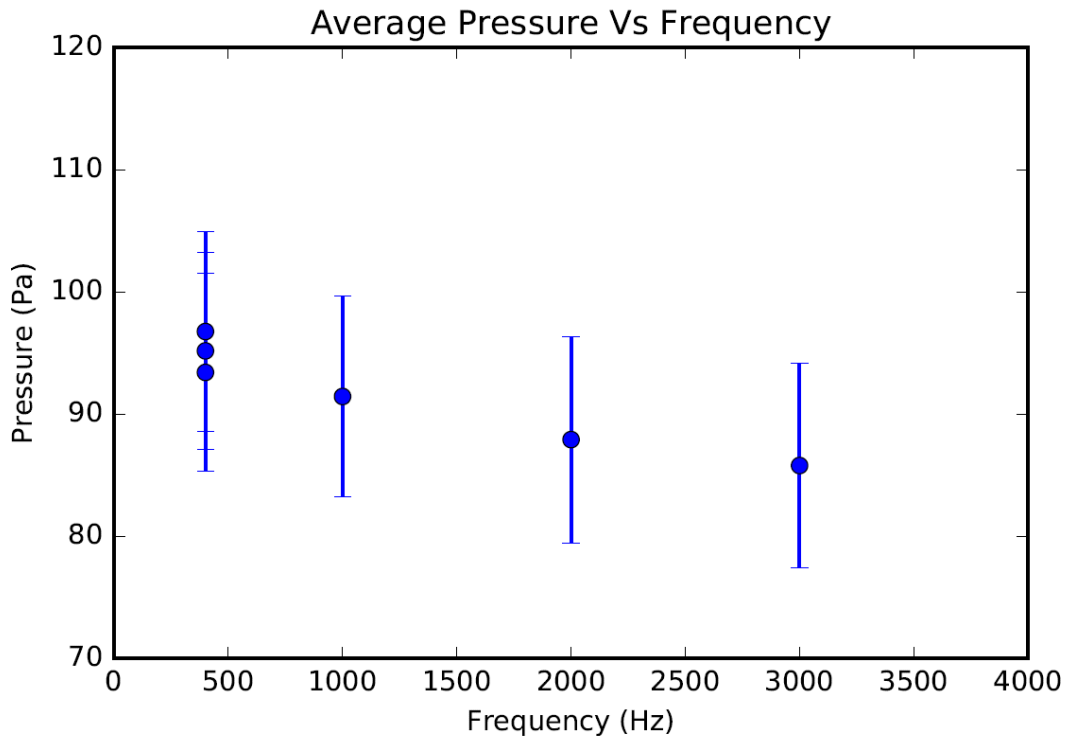


Figure 45: Average pressure for given frequency

The experimental results shown in Figures 44 and 45 exhibit the expected pressure drop when switching to frequencies above 1000 Hz. Based on these results and our previous work with ACEO, our optimal operating frequency is 400 Hz.

The pressure output of the devices increased with decreasing pore diameters as predicted by CFD simulations. The data in Figure 46 shows the maximum pressure outputs for differently sized pores at 120 V_{rms}. With our fabrication limitations, the optimal performance was found at 400 nm pore diameter.

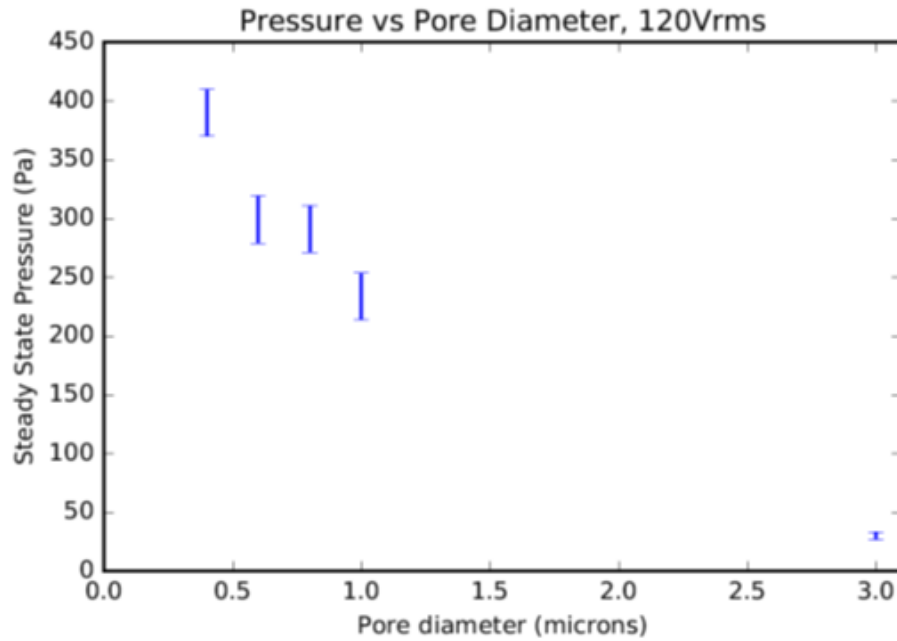


Figure 46: Maximum Pressure vs pore diameter

The continuous pressure increase with the decrease in pore size seems to indicate that smaller sized pores could achieve higher pressure than what we are seeing with the 400 nm pores.

4.4.3 Control Experiments

The polarity of the electrodes was reversed during experimentation. The flow direction remained the same during this reversal which was expected, and helped to rule out DC flow.

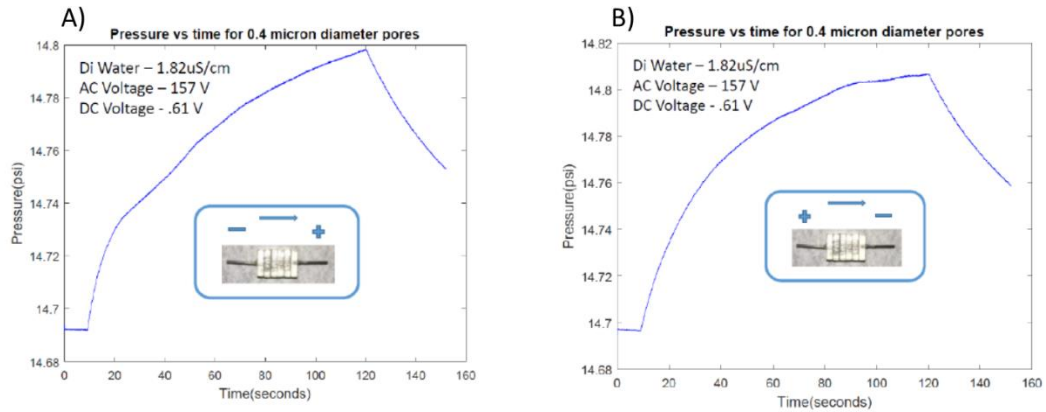


Figure 47: Pressure measurements for control devices A) positive electrode is facing metalized surface B) positive electrode is facing non-metalized surface

As expected, the control experiments did not produce the characteristic pressure profile we saw in typical metalized membrane experimentation.

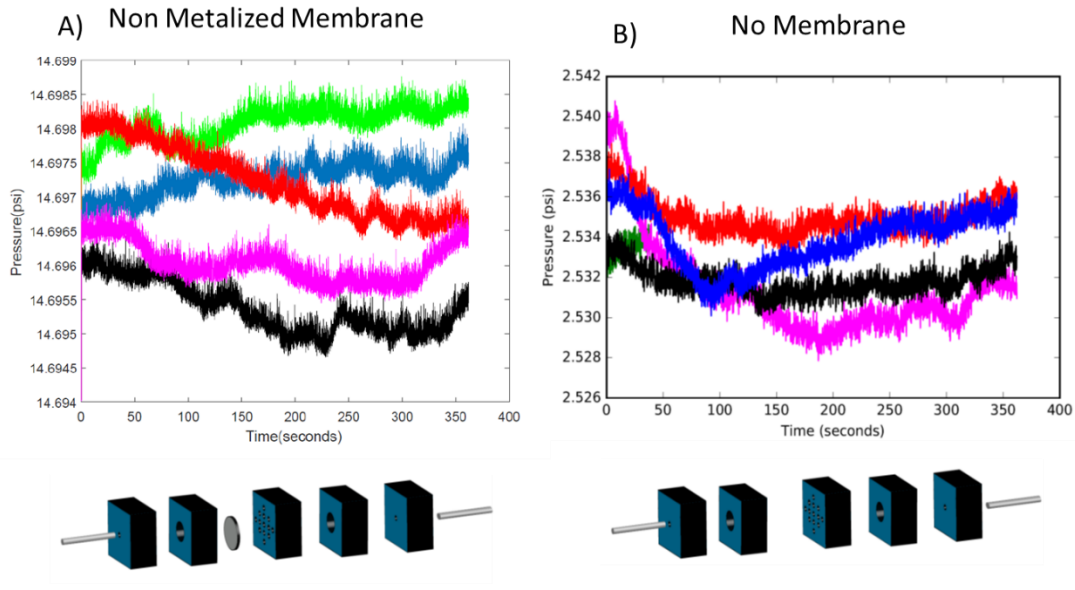


Figure 48: Pressure measurements for control devices A) Device with non-metalized membrane B) Device with no membrane

Both the test devices with a non-metallized membrane and the device with no membrane confirmed that the gold nanostructure is the principal driving factor behind the fluid flow.

The final control experiment was to determine if we were getting fluid flow through the device and not just a pressure change. The experiment was performed by leaving the inlet and outlet open and applying a voltage across the membrane.

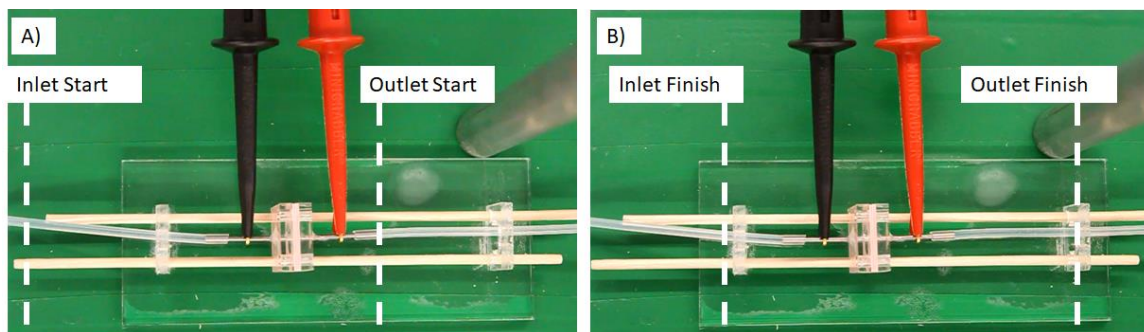


Figure 49: Flow through experiments A) DI water position before applied voltage B) DI water position after applied voltage

The experimental setup can be seen in Figure 49. Figure 49A shows the position of the fluid on the inlet and outlet at the beginning of the experiment, and Figure 49B shows the fluid position at the end of the experiment. The experiment showed the fluid moving from the inlet to the outlet side of the device through the membrane, which validated that there was fluid flow through the device and not just pressure change.

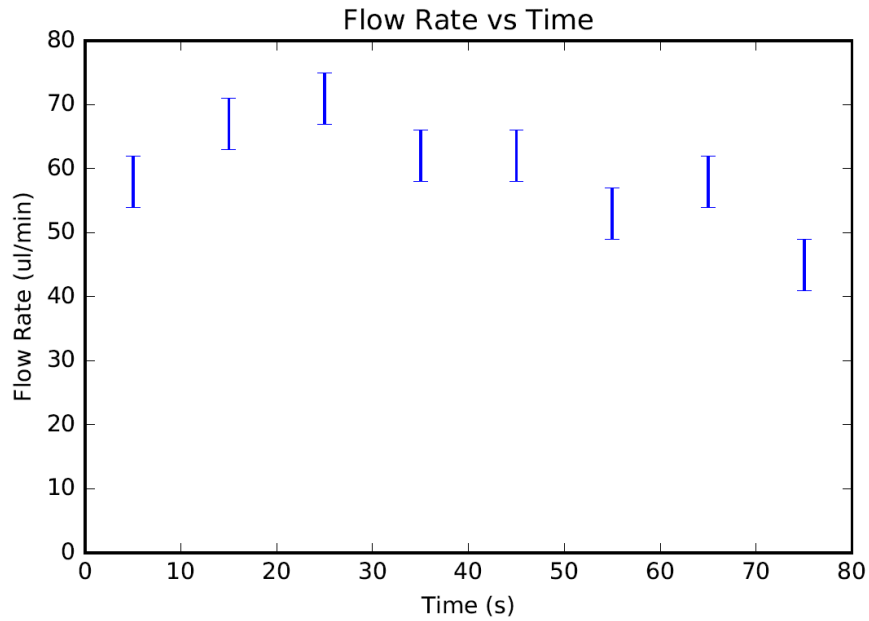


Figure 50: Flow rate vs time for a 400nm membrane at 120V_{rms}

From video analysis it was determined that the flow-through rate in the device was around 60 $\mu\text{L}/\text{min}$. A 400nm membrane at 120V_{rms} was used for these flow experiments because these were the best performing parameters from the pressure experiment. The flow rate over time for these parameters can be seen in Figure 50. The flow-through experiments also indicate that the flow is not generated from bubble formation, since bubbles would push the fluid in both directions.

CHAPTER V:
CONCLUSIONS AND FUTURE WORK

5.1 Light Actuated MEMS - Conclusions

We have shown that GNPs can be incorporated into a functioning MEMS structure with a new fabrication method. This method allows for an exciting new approach which was not previously possible. Chapters 1 and 2 introduce these fabrication processes and chronicle their use in out-of-plane microstructures with embedded GNPs. These structures are able to be actuated wirelessly using GNPs. Applying this technique to the windowpane device, would open up applications in several areas. These windowpane devices could mechanically trigger cardiac cells and nerve cells through the skin without wires. We would be using GNPs which are between 700 nm and 900 nm, well within the Near-Infrared window range. The Near-Infrared window (650-1450 nm) is where light has its deepest penetration into human skin. This method has the potential to be developed into a more robust system for interacting with biological components. Such a system could facilitate research involving mechanical stimulus at the cellular level. Because this new fabrication technique exposes the GNPs to high temperatures, it was important to do a thermal stability study. The thermal stability study allowed us to characterize the behavior of GNPs at higher temperatures. This is important since they melted at much lower temperatures than we have seen in bulk gold, which melts at 1064 C. Additionally, it allowed us to determine factors which are critical to the functionalization of GNPs. Bulk

GNPs show little to no shift in absorbance when they are exposed to temperatures of up to 100 C, which allowed us to determine the safe operating environment for these devices. In addition, we can also say that the 4 watt laser we are using should not have any effect on the functionality of the devices since our experiments in Section 2.2.1 and in previous projects [77] show the devices reaching temperatures below 100 C. Even though the safe operating temperatures of these GNP structures is below 100 C, they can still be used to achieve actuation. These same structures were placed on a hotplate at 100 C and actuation was observed.

While testing the mechanical switching of these structures it was discovered that the flipping behavior strongly correlates to the device side length. After characterizing this behavior, it was determined that this device can also serve as a novel gas flow sensor by taking advantage of its bistability. Although freestanding flow sensors have been created by other groups [78,79] they require constant power and do not provide memory of the flow speeds without an external storage device.

5.2 Light Actuated MEMS- Future work

Although we have shown that we can actuate cantilevers, these cantilevers are of a very basic design. The next step in this project would be to create complex structures like the windowpane that was discussed earlier. Our simulations have shown that selectively heating certain sections of the bistable structure would induce switching between stable states, similar to what we saw with the air flow sensor. The goal would be to have multiple stable shapes that could be “programmed” using a laser. To control local bending, we

would need to map out the spatial pattern of temperature in an illuminated, GNP-patterned device and compare it to models. Temperature depends on GNP shape, density, and the geometry of thin-film structures which are expected to heat more when they are distanced from heat-sinking materials like the silicon substrate. This experiment could be done using the infrared microscope (QFI) in the Shumaker Research Building. One limitation is that the QFI needs planar samples such as bridges tethered on both ends; such test structures are already available on some of the cantilever wafers made in this project.

5.3 Membrane ICEO - Conclusions

We have successfully created metallized membranes for induced charge electroosmotic flow. The flow has been validated by fluorescence video microscopy of membranes using fluorescent tracer beads. The flow response to the AC driving signal has been validated by pressure readings. Pressure ranges are comparable to most conventional ICEO devices, with simpler fabrication. We have also characterized the optimal operating parameters for this fabrication technique. Our experimental results show that the optimal operating parameters are 120 V_{rms} at 400 Hz, with the smallest size membrane being 400nm. Currently we are getting about 400 Pa for a single membrane while microfluidic ACEO devices have achieved pressures at 1300 Pa, but these devices have a larger active volume [80]. With further optimization and our ability to stack the membranes, we believe that we could achieve comparable pressures.

5.4 Membrane ICEO Future Work

Even though the current fabrication technique is reliable and simple, it does still present limitations for how small the membranes can be. We have shown membranes below 400nm get clogged in the sputtering system and cannot be used as a functioning membrane pump. Because of this, future work in this area will have to use other metallization processes like electroless plating. Currently, the applied voltages on the device are relatively high due to the large spacing between the electrodes. Reducing this spacing will drastically lower the needed voltage and improve the overall utility of the devices. Future experiments will also include fluids with higher ionic solutions from .001 mM to 1 mM KCl solution, as these solutions have been shown to have a significant drop-off in the ICEO effect [81]. Preliminary results for stacked membranes have also been performed to determine the feasibility of scaling these devices and achieving higher pressures than possible with a single membrane.

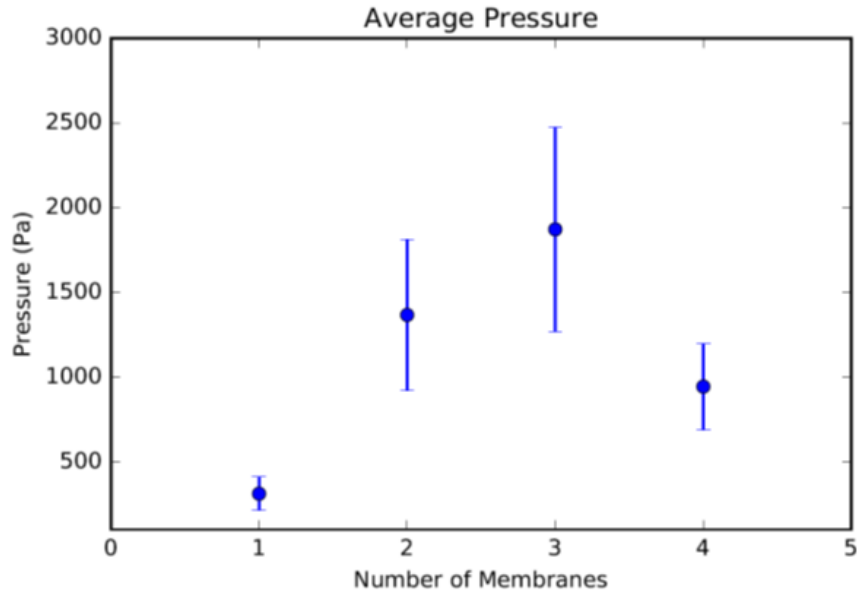


Figure 51: Pressure experiments with multiple membranes

Multiple membranes stacked in the same device do show an increase in pressure. There is a drop off with four membranes, most likely due to the fact that the spacing between the membranes increases and the voltage drop becomes too small to induce pumping. This phenomenon needs to be investigated further since the ability to stack membranes is one of the major benefits of using this flow through geometry. To work around this problem, additional electrodes could be added to the system between the membranes to address the low voltage drop across the electrodes.

5.5 Conclusions- Applications of polarized metallic nanostructures in electric fields

This thesis illustrates how polarized metallic nanostructures can transform electromagnetic energy into other useful forms of energy, such as thermal energy for driving MEMS actuation, and mechanical energy in the form of moving fluids.

These nanostructures were created by self-assembly in the case of the GNPs, or by coating a nanoscale insulating structure with a sputtered gold thin film. In our other previous work [82] three-dimensional small-scale electrodes were produced by metal evaporation at an angle, and in our future work electroless gold plating will be used. These examples show that polarizable nanostructures can be created by a wide array of methods. Their most important feature is their ability to capture electromagnetic energy from a distant source without a direct electrical connection. Such wires would be impractical in the case of a microfluidic device which needs sealing, and impossible in the case of a tissue-embedded MEMS device where wires would provide a route for infection. The two cases here involved significant development of processing that would not disrupt the polarizable nanostructures during device fabrication; examples of integration problems that were

detailed in Chapters II and IV included pore clogging during sputtering, and shifting of the GNP absorption wavelength during subsequent polyimide processing. This thesis addressed limitations of the nanostructure device integration process, and demonstrated viable fabrication pathways toward light-activated multi-stable MEMS as well as AC-driven compact microfluidic pumps. At the end of this project two important goals were achieved. First, by moving our previous fabrication process from metal to polyimide the thermal contrast between GNP and non-GNP cantilevers within a close proximity was shown to be possible. The second project successfully demonstrated ICEO pumping through a metallized membrane.

REFERENCES

- [1] Goessling, B. A., et al. "Bistable out-of-plane stress-mismatched thermally actuated bilayer devices with large deflection." *Journal of Micromechanics and Microengineering* 21.6 (2011): 065030.
- [2] Vaccaro, Pablo O., Kazuyoshi Kubota, and Tahito Aida. "Strain-driven self-positioning of micromachined structures." *Applied Physics Letters* 78.19 (2001): 2852-2854.
- [3] Moiseeva, E., et al. "Single-mask microfabrication of three-dimensional objects from strained bimorphs." *Journal of Micromechanics and Microengineering* 17.9 (2007): N63.
- [4] Overvelde, Johannes TB, et al. "A three-dimensional actuated origami-inspired transformable metamaterial with multiple degrees of freedom." *Nature communications* 7 (2016).
- [5] Raney, Jordan R., et al. "Stable propagation of mechanical signals in soft media using stored elastic energy." *Proceedings of the National Academy of Sciences* (2016): 201604838.
- [6] Ion, Alexandra, Ludwig Wall, Robert Kovacs, and Patrick Baudisch. "Digital Mechanical Metamaterials." In *Proceedings of the 2017 CHI Conference on Human Factors in Computing Systems*, pp. 977-988. ACM, 2017.

- [7] Beharic, J., T. M. Lucas, and C. K. Harnett. "Analysis of a Compressed Bistable Buckled Beam on a Flexible Support." *Journal of Applied Mechanics* 81, no. 8 (2014): 081011
- [8] Receveur, Rogier AM, et al. "Laterally moving bistable MEMS DC switch for biomedical applications." *Journal of microelectromechanical systems* 14.5 (2005): 1089-1098.
- [9] Wu, Y. B., et al. "Magnetostatic bistable MEMS switch with electrothermal actuators." *Electronics letters* 46.15 (2010): 1074-1075.
- [10] Qui, J., et al. "A high-current electrothermal bistable MEMS relay." *Micro Electro Mechanical Systems, 2003. MEMS-03 Kyoto. IEEE The Sixteenth Annual International Conference on. IEEE, 2003.*
- [11] Ando, Bruno, et al. "Investigation on mechanically bistable MEMS devices for energy harvesting from vibrations." *Journal of Microelectromechanical Systems* 21.4 (2012): 779-790.
- [12] Lucas, T. M., et al. "Bistability in a symmetric out-of-plane microstructure." *Microsystem Technologies* 23.7 (2017): 2569-2576.
- [13] Gobin, André M., et al. "Near-infrared resonant nanoshells for combined optical imaging and photothermal cancer therapy." *Nano letters* 7.7 (2007): 1929-1934.
- [14] Huang, Xiaohua, et al. "Cancer cell imaging and photothermal therapy in the near-infrared region by using gold nanorods." *Journal of the American Chemical Society* 128.6 (2006): 2115-2120.

- [15] Ghosh, Partha, et al. "Gold nanoparticles in delivery applications." *Advanced drug delivery reviews* 60.11 (2008): 1307-1315. [16] Han, Gang, et al. "Drug and gene delivery using gold nanoparticles." *Nanobiotechnology* 3.1 (2007): 40-45.
- [17] Willets, K. A., & Van Duyne, R. P. (2007). Localized surface plasmon resonance spectroscopy and sensing. *Annu. Rev. Phys. Chem.*, 58, 267-297.
- [18] Hososhima, Shoko, et al. "Near-infrared (NIR) up-conversion optogenetics." *Scientific reports* 5 (2015).
- [19] Gao, X., Cui, Y., Levenson, R. M., Chung, L. W., & Nie, S. (2004). In vivo cancer targeting and imaging with semiconductor quantum dots. *Nature Biotechnology*, 22(8), 969-976. doi:10.1038/nbt994
- [20] Brann, Tyler. *Synthesis of a drug delivery vehicle for cancer treatment utilizing DNA-functionalized gold nanoparticles*. University of Louisville, 2014.
- [21] Wilson, Robert. "The use of gold nanoparticles in diagnostics and detection." *Chemical Society Reviews* 37.9 (2008): 2028-2045.
- [22] Jana, Nikhil R., Latha Gearheart, and Catherine J. Murphy. "Seed-mediated growth approach for shapecontrolled synthesis of spheroidal and rod-like gold nanoparticles using a surfactant template." *Advanced Materials* 13.18 (2001): 1389.
- [23] Jain, Prashant K., Susie Eustis, and Mostafa A. El-Sayed. "Plasmon coupling in nanorod assemblies: optical absorption, discrete dipole approximation simulation, and exciton-coupling model." *The Journal of Physical Chemistry B* 10.37 (2006): 18243-18253.

- [24] Scarabelli, Leonardo, et al. "Monodisperse gold nanotriangles: size control, large-scale self-assembly, and performance in surface-enhanced Raman scattering." *ACS nano* 8.6 (2014): 5833-5842.
- [25] Beeram, Srinivas R., and Francis P. Zamborini. "Selective attachment of antibodies to the edges of gold nanostructures for enhanced localized surface plasmon resonance biosensing." *Journal of the American Chemical Society* 131.33 (2009): 11689-11691.
- [26] Njoki, Peter N., et al. "Size correlation of optical and spectroscopic properties for gold nanoparticles." *The Journal of Physical Chemistry C* 111.40 (2007): 14664-14669.
- [27] Link, S., & El-Sayed, M. A. (1999). Size and Temperature Dependence of the Plasmon Absorption of Colloidal Gold Nanoparticles. *The Journal of Physical Chemistry B*, 103(21), 4212-4217. doi:10.1021/jp984796o
- [28] Link, S., Mohamed, M. B., & El-Sayed, M. A. (1999). Simulation of the optical absorption spectra of gold nanorods as a function of their aspect ratio and the effect of the medium dielectric constant. *The Journal of Physical Chemistry B*, 103(16), 3073-3077.
- [29] Link, S., Mohamed, M. B., & El-Sayed, M. A. (1999). Simulation of the optical absorption spectra of gold nanorods as a function of their aspect ratio and the effect of the medium dielectric constant. *The Journal of Physical Chemistry B*, 103(16), 3073-3077.
- [30] Link, S., Mohamed, M. B., & El-Sayed, M. A. (1999). Simulation of the optical absorption spectra of gold nanorods as a function of their aspect ratio and the effect of the medium dielectric constant. *The Journal of Physical Chemistry B*, 103(16), 3073-3077.
- [31] Draine, B. T., & Flatau, P. J. (1994). Discrete-dipole approximation for scattering calculations. *JOSA A*, 11(4), 1491- 1499.

- [32] Kelly, K. Lance, Eduardo Coronado, Lin Lin Zhao, and George C. Schatz. "The optical properties of metal nanoparticles: the influence of size, shape, and dielectric environment." *The Journal of Physical Chemistry B* 107, no. 3 (2003): 668-677.
- [33] Hao, E., Schatz, G. C., & Hupp, J. T. (2004). Synthesis and optical properties of anisotropic metal nanoparticles. *Journal of Fluorescence*, 14(4), 331-341.
- [34] James, K. T., et al. "EFFECT OF MOLECULAR WEIGHT CUT-OFF OF CELLULOSE MEMBRANES ON HIGH YIELD PRODUCTION OF GOLD/GOLD SULFIDE NANOPARTICLES."
- [35] Yu, Yanlei, Makoto Nakano, and Tomiki Ikeda. "Photomechanics: directed bending of a polymer film by light." *Nature* 425.6954 (2003): 145-145. [36] Han, Li-Hsin, et al. "Light-powered micromotor driven by geometry-assisted, asymmetric photon-heating and subsequent gas convection." *Applied Physics Letters* 96.21 (2010): 213509.
- [37] Santini, J. T., Cima, M. J., & Langer, R. (1999). A controlled-release microchip. *Nature*, 397(6717), 335-338.
- [38] Lucas, T. M., James, K. T., Beharic, J., Moiseeva, E. V., Keynton, R. S., Otoole, M. G., & Harnett, C. K. (2014). Wavelength specific excitation of gold nanoparticle thin-films. *Applied Physics Letters*, 104(1), 011909. doi:10.1063/1.4861603
- [39] S.Y. Xiao, L.F. Che, X.X. Li, Y.L. Wang, A novel fabrication process of MEMS devices on polyimide flexible substrates, *Microelectronic Engineering*, Volume 85, Issue 2, 2008, Pages 452-457, ISSN 0167-9317, <http://dx.doi.org/10.1016/j.mee.2007.08.004>. (<http://www.sciencedirect.com/science/article/pii/S0167931707006582>)

- [40] G. M. Atkinson et al., "Novel piezoelectric polyimide MEMS," TRANSDUCERS, Solid-State Sensors, Actuators and Microsystems, 12th International Conference on, 2003, Boston, MA, USA, 2003, pp. 782-785 vol.1.
- [41] Kim, Ji-Hong, et al. "High sensitivity capacitive humidity sensor with a novel polyimide design fabricated by MEMS technology." Nano/Micro Engineered and Molecular Systems, 2009. NEMS 2009. 4th IEEE International Conference on. IEEE, 2009.
- [42] Karen C. Cheung, Philippe Renaud, Heikki Tanila, Kaj Djupsund, Flexible polyimide microelectrode array for in vivo recordings and current source density analysis, Biosensors and Bioelectronics, Volume 22, Issue 8, 2007, Pages 1783-1790, ISSN 0956-5663
- [43] Petrova, Hristina, et al. "On the temperature stability of gold nanorods: comparison between thermal and ultrafast laser-induced heating." Physical Chemistry Chemical Physics 8.7 (2006): 814-821.
- [44] Draine, B.T., & Flatau, P.J. 1994, "Discrete dipole approximation for scattering calculations", J. Opt. Soc. Am. A, 11, 1491-1499
- [45] Draine, B.T., & Flatau, P.J. 2012, "User Guide to the Discrete Dipole Approximation Code DDSCAT 7.2"
- [46] Draine, B.T., & Flatau, P.J., "Discrete-dipole approximation for periodic targets: theory and tests", J. Opt. Soc. Am. A, 25, 2593-2703 (2008)
- [47] Flatau, P.J., & Draine, B.T., "Fast near-field calculations in the discrete dipole approximation for regular rectilinear grids", Optics Express, 20, 1247-1252 (2012)

- [48] AbderRahman N Sobh; Sarah White; Jeremy Smith; Nahil Sobh; Prashant K Jain (2016), "nanoDDSCAT+," <https://nanohub.org/resources/ddaplus>. (DOI: 10.4231/D3KH0F08T).
- [49] Fang, Ai Qin, et al. "Regioselective plasmonic coupling in metamolecular analogs of benzene derivatives." *Nano letters* 15.1 (2014): 542-548.
- [50] Sun, Qi-C., et al. "Copper plasmonics and catalysis: role of electron-phonon interactions in dephasing localized surface plasmons." *Nanoscale* 6.21 (2014): 12450-12457.
- [51] Hubbard, R. L., et al. "Low temperature curing of polyimide wafer coatings." *Electronics Manufacturing Technology Symposium, 2004. IEEE/CPMT/SEMI 29th International*. IEEE, 2004.
- [52] Bazant, M. Z., & Squires, T. M. (2004). Induced-charge electrokinetic phenomena: theory and microfluidic applications. *Physical Review Letters*, 92(6), 066101.
- [53] Antonio Ramos, Hywel Morgan, Nicolas G Green, Antonio Castellanos, AC Electric-Field-Induced Fluid Flow in Microelectrodes, *Journal of Colloid and Interface Science*, Volume 217, Issue 2, 1999, Pages 420-422, ISSN 0021-9797, <http://dx.doi.org/10.1006/jcis.1999.6346>.
- [54] Harnett, Cindy K., Jeremy Templeton, Katherine A. Dunphy-Guzman, Yehya M. Senousy, and Michael P. Kanouff. 2008. "Model Based Design of a Microfluidic Mixer Driven by Induced Charge Electroosmosis." *Lab on a Chip* 8 (4): 565-72.

- [55] Kovarik, M. L. and Jacobson, S. C., "Integrated Nanopore/Microchannel Devices for Ac Electrokinetic Trapping of Particles." *Analytical Chemistry* 80, no. 3, 657–64, 2008.
- [56] Ulbricht, M., "Advanced Functional Polymer Membranes." *Polymer* 47, no. 7, 2217–62, 2006.
- [57] Volpatti, Lisa R., and Ali K. Yetisen. "Commercialization of microfluidic devices." *Trends in biotechnology* 32.7 (2014): 347-350.
- [58] Laser, Daniel J., and Juan G. Santiago. "A review of micropumps." *Journal of micromechanics and microengineering* 14.6 (2004): R35.
- [59] Whitney, J. P., Glisson, M. F., Brockmeyer, E. L., and Hodgins, J. K., "A Low-Friction Passive Fluid Transmission and Fluid-Tendon Soft Actuator," *Proc. IEEE/RSJ International Conference on Intelligent Robots and Systems (IROS)*, Chicago, IL September 14-18, 2014.
- [60] Shepherd, R. F., Ilievski, F., Choi, W., Morin, S. A., Stokes, A. A., Mazzeo, A. D., Chen, X., Wang, M., and Whitesides. "Multigait Soft Robot." *Proceedings of the National Academy of Sciences of the United States of America* 108, no. 51, 20400–403, 2011.
- [61] Squires, T. M., and Bazant, M. Z., "Induced-charge electro-osmosis." *Journal of Fluid Mechanics* 509, 217-252, 2004.
- [62] Siwy, Z. S. "Ion-Current Rectification in Nanopores and Nanotubes with Broken Symmetry." *Advanced Functional Materials* 16, no. 6, 735-746, 2006.

- [63] Siwy, Z., Heins, E., Harrell, C. C., Kohli, P., and Martin, C. R., "Conical-Nanotube Ion-Current Rectifiers: The Role of Surface Charge." *Journal of the American Chemical Society* 126, no. 35, 10850– 51, 2004.
- [64] Schoch, R. B., Han, J., and Renaud, P., "Transport phenomena in nanofluidics." *Reviews of Modern Physics* 80 no.3, 839, 2008.
- [65] C. C. Huang, M. Z. Bazant and T. Thorsen, Ultrafast high- pressure AC electro-osmotic pumps for portable biomedical microfluidics, *Lab Chip*, 2009, 10(1), 80–85.
- [66] Bazant, M. Z., & Squires, T. M. (2004). Induced-charge electrokinetic phenomena: theory and microfluidic applications. *Physical Review Letters*,92(6), 066101.
- [67] C. K.Harnett, Jeremy Templeton, Katherine A.Dunphy-Guzman, Yehya M.Senousy, and Michael P.Kanouff, *Lab on a Chip*, 8 , Pages 565-572, 2008
- [68] Bazant, M. Z., Kilic, M. S., Storey, B. D., & Ajdari, A. (2009). Towards an understanding of induced-charge electrokinetics at large applied voltages in concentrated solutions. *Advances in Colloid and Interface Science*, 152(1-2), 48-88.
- [69] Bazant, M. Z., Kilic, M. S., Storey, B. D., & Ajdari, A. (2009). Towards an understanding of induced-charge electrokinetics at large applied voltages in concentrated solutions. *Advances in Colloid and Interface Science*, 152(1-2), 48-88.
- [70] Huang, C., Bazant, M. Z., & Thorsen, T. (2010). Ultrafast high-pressure AC electro-osmotic pumps for portable biomedical microfluidics. *Lab Chip*, 10(1), 80-85.
- [71] Wu, Xiaojian, Pradeep Ramiah Rajasekaran, and Charles R. Martin. "An alternating current electroosmotic pump based on conical nanopore membranes." (2016).

- [72] Paustian, Joel S., et al. "Induced charge electroosmosis micropumps using arrays of Janus micropillars." *Lab on a Chip* 14.17 (2014): 3300-3312.
- [73] Yao, Shuhuai, and Juan G. Santiago. "Porous glass electroosmotic pumps: theory." *Journal of Colloid and Interface Science* 268.1 (2003): 133-142.
- [74] Yao, Shuhuai, et al. "Porous glass electroosmotic pumps: design and experiments." *Journal of Colloid and Interface Science* 268.1 (2003): 143-153.
- [75] Harnett, Cindy K., Jeremy Templeton, Katherine A. Dunphy-Guzman, Yehya M. Senousy, and Michael P. Kanouff. 2008. "Model Based Design of a Microfluidic Mixer Driven by Induced Charge Electroosmosis." *Lab on a Chip* 8 (4): 565-72
- [76] Bazant, Martin Z., et al. "Towards an understanding of induced-charge electrokinetics at large applied voltages in concentrated solutions." *Advances in colloid and interface science* 152.1 (2009): 48-88.
- [77] Lucas, Thomas M., et al. "Thermal properties of infrared absorbent gold nanoparticle coatings for MEMS applications." *Sensors and Actuators A: Physical* 198 (2013): 81-86.
- [78] Wang, Yu-Hsiang, Chia-Yen Lee, and Che-Ming Chiang. "A MEMS-based air flow sensor with a free-standing microcantilever structure." *Sensors* 7.10 (2007): 2389-2401.
- [79] Parcell, James, et al. "A novel air flow sensor from printed PEDOT micro-hairs." *Smart Materials and Structures* 22.11 (2013): 112001.
- [80] Huang, C., Bazant, M. Z., & Thorsen, T. (2010). Ultrafast high-pressure AC electro-osmotic pumps for portable biomedical microfluidics. *Lab Chip*, 10(1), 80-85.

[81] Bazant, M. Z., Kilic, M. S., Storey, B. D., & Ajdari, A. (2009). Towards an understanding of induced-charge electrokinetics at large applied voltages in concentrated solutions. *Advances in Colloid and Interface Science*, 152(1-2), 48-88.

[82] Senousy, Y. M., and C. K. Harnett. 2010. "Fast Three Dimensional Ac Electro-Osmotic Pumps with Nonphotolithographic Electrode Patterning." *Biomicrofluidics* 4 (3). <http://doi.org/10.1063/1.3463719>.

APPENDIX A

FEA Modeling of Window Pane Device

ANSYS v14.5 was used to evaluate static buckled out of plane heights, natural frequencies, Von Mises Stresses, buckling forces, and various spring constants. SHELL281 elements with midside nodes are used to model the device due to its very thin features. Layered sections composing of 500 μm and 95 nm of SiO₂ and platinum respectively are used to create the overall structure of the device. Other material properties used for the FEA analysis are shown in Table 1 below.

Table 1. Geometric and material property values used in ANSYS.

	SiO ₂	Platinum
Thickness (nm)	500	95
Density (kg/m ³)	2,648	21,450
Young's Modulus (MPa)	73	170
Poisson's Ratio	0.2	0.3
Fictitious CTE (m/m*C)	4e-6	0

Before any modal or structural behavior aspects can be obtained the device needs to exhibit buckling due to a relatively large stress induced by the SiO₂. To do this in ANSYS a fictitious CTE is used for the SiO₂ while leaving the CTE for platinum at zero. A rectangular shape (10 x 0.5 μm) populated with PLANE183 elements and an axisymmetric analysis are used to plot radial stress versus change in temperature. Boundary conditions on the disk include no displacement on the bottom and left/right side. Radial stress measurements are taken at the center of the rectangle. Since the thermally grown oxide for these devices is measured using a Toho thin film stress system and results in 300 MPa biaxial stress, the delta temperature used to emulate the stress for the FEA is 820 C.

The center of the device has a boundary condition of being fully clamped. Before any external loads on the device is are applied, buckling must occur in three load steps. The first load step is to apply a small pressure perturbation which will influence the initial direction of buckling. Applying the thermal temperature difference of 820C is the second load step and is done over 400 substeps. Finally, the initial perturbation pressure is

removed for load step three and the FEA model now sits in the static buckled form as shown in Figure 1 below.

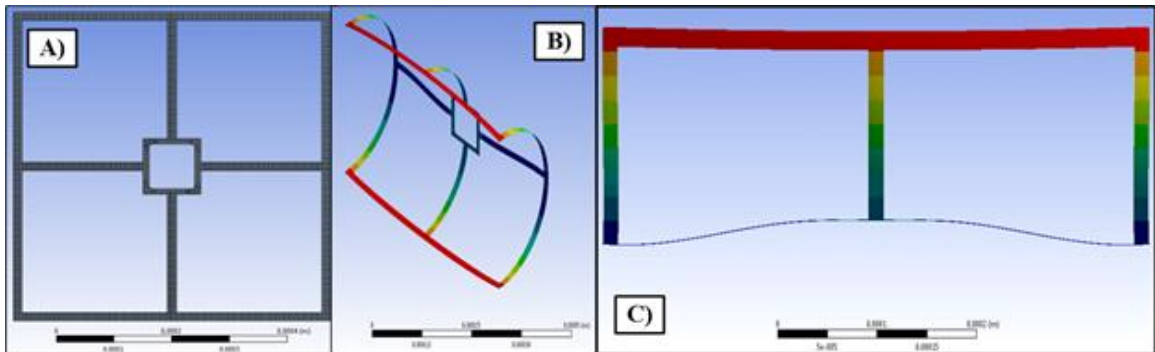


Figure 1. A) Mesh and B, C) static buckled profile for the 550 μm window device.

Stiffness of the device was tested in load step four using 400 substeps. The applied force had a magnitude of 10 μN and was kept in either the X or Z (sideways or upper) global coordinate direction which means it does not change orientation with the local element coordinate system. As a first approximation the stiffness of the structure, in respect to the applied force, can be evaluated as the magnitude of the load divided by the distance traversed by at the location the load is applied. Examples of the structure under load to analyze stiffness is shown in Figure 2 below. Displacement of the structure under load is not entirely linear. This can be observed via a plot of horizontal displacement versus horizontal force for Figure 2 B) shown in Figure 3 below.

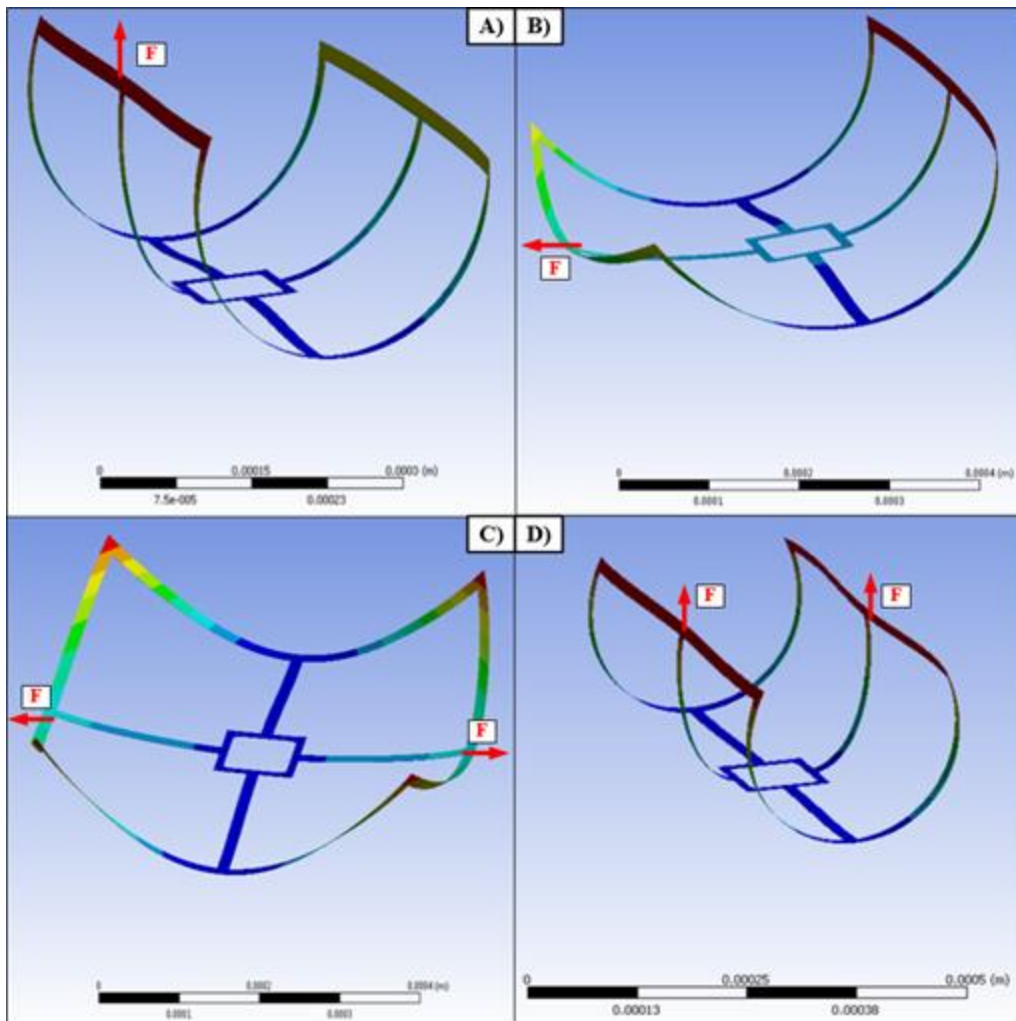


Figure 2. External applied loads to the 550 μm buckled device in the A) Z direction single force, B) Sideways single force, C) Sideways double force, and D) Z direction double force.

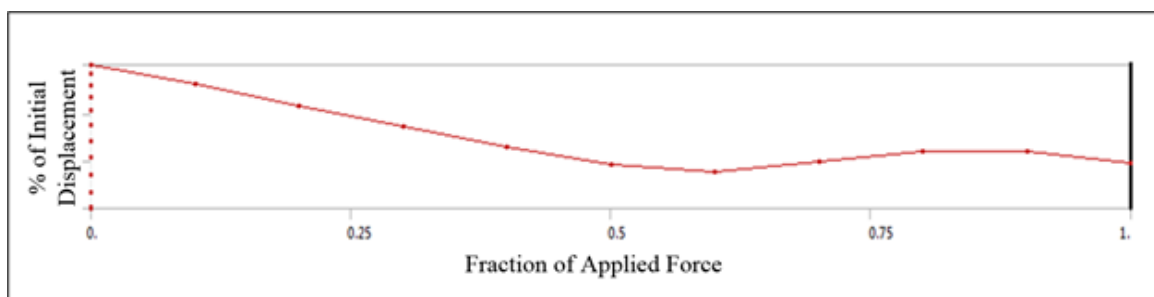


Figure 3. Displacement versus force for a sideways loaded single force device.

Modal analysis for the first 6 mode shapes was done after a static displacement buckling solution with all excitation frequencies being in the kHz region. Another analysis is the force need for the device to “snap-through” to another stable buckled shape. A force of 10 μN was applied in the upward direction on the lower beam. As snap-through occurs, a rapid transition of geometry is observed and can be monitored by a force versus displacement graph. All of these force location, stable geometry just before snap-through, and a force versus displacement graph can be seen in Figure 4 below.

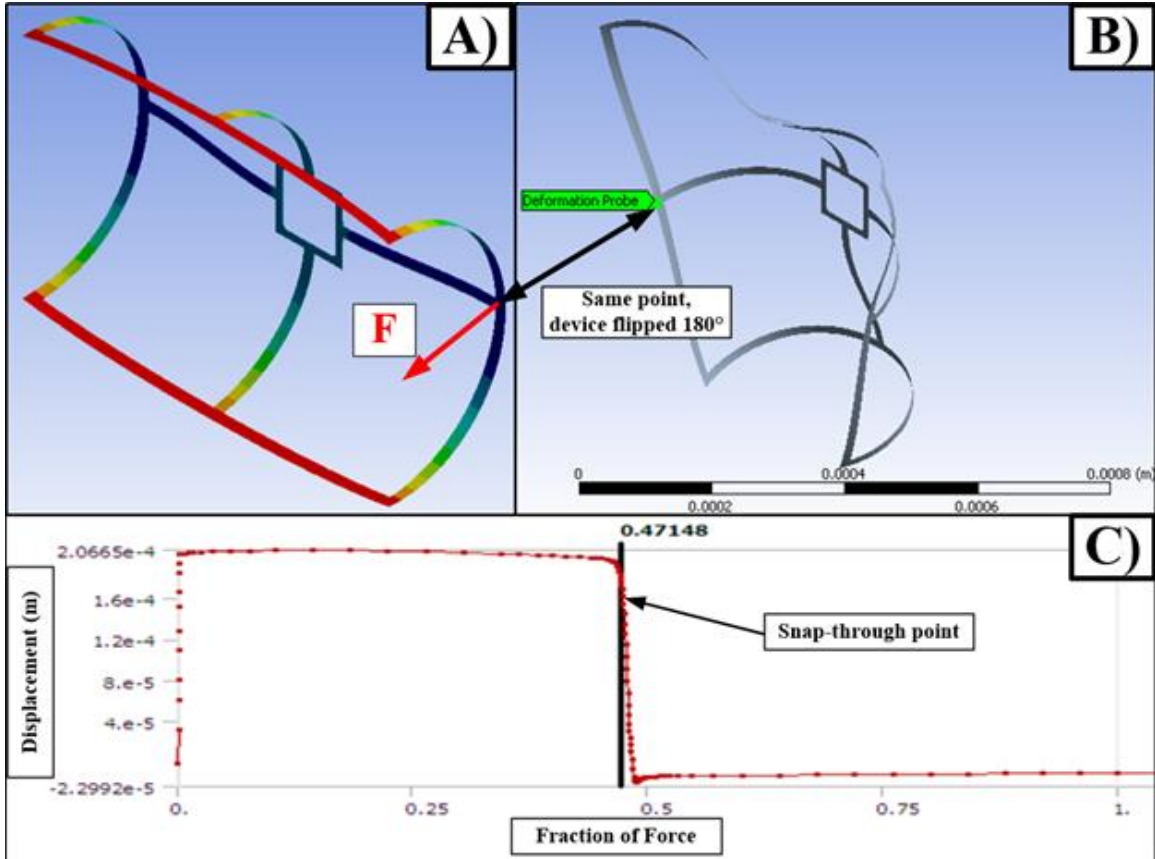


Figure 4. Snap-through analysis A) applied force location, B) displacement probe and geometry just before snap-through, and C) a graph of force versus displacement.

"

"

CURRICULUM VITAE

"

Jasmin Beharic

Louisville, KY

Phone: (502)396-9548

Email: j0beha01@louisville.edu

Summary

Available: August 2017

Areas of focus in graduate career:

- Microelectromechanical Systems (MEMS) Design
- Microfluidic and Environmental Sensor Applications

- Experienced with working in teams to accomplish objectives

- Trained in many MEMS fabrication techniques including: Lithography, Thin-film Deposition, Thermal Processing, Wet and Dry Etching, Metrology and Testing, SEM Imaging

- Software proficiency: Matlab, L-Edit, Coventorware, Silvaco (Athena, Atlas), LabVIEW, ANSYS, Microsoft Office Products

Education

Ph.D. in in Electrical and Computer Engineering

August 2017

University of Louisville, Speed School of Engineering, Louisville, KY

Focus: Focus on incorporating nanoparticles into MEMS fabrication for new functionality

M.Eng. Degree in Electrical and Computer Engineering

May 2012

University of Louisville, Speed School of Engineering, Louisville, KY

B.S. Degree in Electrical and Computer Engineering

August 2011

University of Louisville, Speed School of Engineering, Louisville, KY

Publications

Lucas, T. M., James, K. T., **Beharic, J.**, Moiseeva, E. V., O'Toole, M. G., Harnett, C. K., "Wavelength specific excitation of gold nanoparticle thin-films", *Appl. Phys. Lett.* 104 (2014)

J. Beharic, T. M. Lucas, C. K. Harnett, 'Analysis of a Compressed Bistable Buckled Beam on a Flexible Support', *Journal of Applied Mechanics*, Aug 2014

Lucas, T. M., Porter, D. A., **Beharic, J.**, Berfield, T. A., & Harnett, C. K. (2017). Bistability in a symmetric out-of-plane microstructure. *Microsystem Technologies*, 23(7), 2569-2576.

Conference Presentations

Beharic, J., James, K. T., Moiseeva, E. V., Lucas, T. M., Keynton, R. S., O'Toole, M. G., and Harnett, C. K., "Patterning Gold Nano Particles for Enhancing Light-Induced Thermal Actuation", 10th KY Innovation Entrepreneurship Conference, Louisville Ky., September 2014 *Poster*

Jasmin Beharic, Yehya M. Senusy, Thomas M. Lucas, Cindy K. Harnett, "Flexible Sensors for Shape Detection", KY NanoSymposium 2013, University of Louisville, Kentucky, August 16-17 2013 *Poster*

T. M. Lucas, **J. Beharic**, Y. M. Senousy, E. V. Moiseeva, C. K. Harnett, *Presentation*
“Characterization of a Bistable Microstructure for Bidirectional Air Flow
Threshold Sensing”, KY NanoSymposium 2013, University of Louisville,
Kentucky, August 16-17 2013

J. Beharic, Y. M. Senousy, C. K. Harnett, “Experimental and analytical *Presentation*
investigation of metalized porous membranes for induced-charge electrokinetic *and Poster*
flows”, Gordon Research Conferences 2015, Vermont, August 16-17 2013